IOP Publishing Quantum Sci. Technol. 10 (2025) 035029 https://doi.org/10.1088/2058-9565/add8b6

Quantum Science and Technology

OPEN ACCESS

RECEIVED
30 January 2025

REVISED
30 April 2025

ACCEPTED FOR PUBLICATION
14 May 2025

PUBLISHED
27 May 2025

PAPER

Benchmarking digital–analog quantum computation for the inhomogeneous two-body Ising model

Vicente Pina Canelles[1,2,*], **Manuel G Algaba**[1], **Hermanni Heimonen**[3], **Miha Papič**[1,2], **Mario Ponce**[1,2], **Jami Rönkkö**[3], **Manish J Thapa**[1], **Inés de Vega**[1,2] **and Adrian Auer**[1]

[1] IQM Germany GmbH, Georg-Brauchle-Ring 23-25, 80992 Munich, Germany
[2] Department of Physics and Arnold Sommerfeld Center for Theoretical Physics, Ludwig-Maximilians-Universität München, Theresienstrasse 37, 80333 Munich, Germany
[3] IQM Finland Oy, Keilaranta 19, 02150 Espoo, Finland
[*] Author to whom any correspondence should be addressed.

E-mail: vicente.pina@meetiqm.com

Keywords: quantum computing, quantum information, digital–analog quantum computation

Abstract

Digital–analog quantum computation (DAQC) has recently been proposed as an alternative to the standard paradigm of digital quantum computation (DQC). DAQC generates entanglement through a continuous or analog evolution of the whole device, rather than by applying two-qubit gates. This manuscript describes an in-depth analysis of errors in DAQC implementing Ising Hamiltonians used for arbitrary computations, which was missing from the previous literature, revealing that, overall, DAQC errors scale less favorably compared to those in DQC. As demonstrated, for an all-to-all connectivity, the leading error source for DAQC scales like $\Theta(N^4)$, while for the digital case, it scales like $\mathcal{O}(N^2)$ for implementing an arbitrary Hamiltonian evolution. We further illustrate this result with our own simulations of the Quantum Fourier Transform, which in the previous literature were based on unrealistic parameter choices, biasing the result in favor of DAQC, and were limited to system sizes of up to only seven qubits. On the other hand, we develop a specific DAQC protocol for a star connectivity, which shows an advantage for the particular case of a GHZ state generation protocol.

1. Introduction

Digital–analog quantum computation (DAQC) has recently emerged as a new paradigm for quantum computation [1–7], posing an alternative to standard digital quantum computation (DQC). DAQC is compelling because it combines the natural evolution of a quantum device, generated by a given entangling Hamiltonian, with engineered control only over single-qubit gates (SQGs) to perform quantum computations. The working assumption is that the analog evolution of the device is more robust against control errors than two-qubit gates (TQGs) [8], which are the typical entangling operations utilized in DQC. DAQC has been claimed to be more resilient to noise and faster than DQC, e.g for implementing the quantum Fourier transform (QFT) routine [4, 5].

In this manuscript, we revisit these statements by performing the first detailed analysis of error scaling in DAQC for the inhomogeneous Ising model (which is the universal DAQC technique used in [1–7]), considering important sources such as control errors due to an imperfect characterization of the analog Hamiltonian. We also study for the first time the scaling of depth in quantum algorithms when implemented with Ising DAQC. While the error scaling is dependent on the connectivity of the device, our analysis is applicable to any connectivity. Specifically, for an all-to-all (ATA) qubit connectivity, we find that, while any two-qubit Hamiltonian can be implemented using at most $\mathcal{O}(N^2)$ TQGs in DQC, DAQC introduces, in general, $\Theta(N^4)$ two-qubit terms which are prone to error. These scalings are valid for generic quantum algorithms, and they arise precisely from the fact that the analog evolution comprises all qubits. Therefore,

our analysis concludes that the scaling of errors in DAQC is fundamentally worse than in DQC for arbitrary algorithms. We apply this analysis to the specific case of the QFT, finding that DQC requires $\Theta(N^2)$ two-qubit terms for the full algorithm while DAQC introduces $\Theta(N^5)$. We also find that the execution time of the QFT circuit for DAQC is $\Theta(N^{2.05})$, considerably worse than for DQC, for which execution time scales as $\Theta(N)$. We confirm these results with simulation.

Thus, while Ising DAQC is often portrayed in the literature as a promising alternative to the digital case, we counter this view by presenting the first comprehensive analysis of its scaling properties, its execution speed, and of the impact of errors on its performance as compared to the digital approach. As argued in [9] these factors are essential for evaluating the performance of quantum computation in the NISQ era. Previous studies on DAQC, particularly those regarding the digital–analog QFT [4–6], have relied predominantly on simulations where chosen gate parameters favored DAQC and which were limited to very small system sizes, preventing a rigorous comparison. Additionally, in this manuscript, we refute claims that DAQC 'can enhance the depth of the implementation of a quantum algorithm [QFT]' [4]. By demonstrating that DAQC has a significantly faster error scaling than digital, we show how it underperforms DQC even for relatively small devices. We further confirm this result by conducting simulations based on realistic parameters, thus uncovering fundamental limitations in DAQC for the Ising model compared to DQC.

In this manuscript: (i) we provide an analysis of the error scaling of Ising DAQC with the number of qubits of the device, considering a detailed account of the number of operations introduced, and identifying and accounting for major sources of error. This analysis is valid for any algorithm or device connectivity. (ii) Using this analysis, we study the scaling of errors when implementing the QFT routine using DAQC in an ATA connectivity, and conclude that it is extremely unfavorable with respect to its digital version, refuting previous claims found in [4, 5]. (iii) We demonstrate that, under certain specific conditions—related to both the protocol and the connectivity of the architecture—DAQC can be implemented with a minimal number of analog blocks, significantly enhancing its performance. This is exemplified through the generation of GHZ states on a tailored star architecture, where only a single analog block is required, allowing DAQC to scale favorably compared to the digital approach. (iv) We confirm our results both analytically and with numerical simulations. Throughout our study, we consider the two versions of DAQC proposed in the literature: stepwise DAQC, consisting of a sequential approach where all the interactions are simultaneously switched on and off between layers of single qubit gates, simplifying the theoretical analysis, and banged DAQC, where an always-on multi-qubit interaction is overlapped with fast single-qubit pulses.

2. Problem statement

In this section, we sketch a brief explanation of the DAQC method described in [1], which is the basis for the methods in [2, 3] and further used for the digital–analog algorithms studied in [4–7][4]. For a more detailed explanation of the method, we direct the reader to appendix A.

We assume that we can physically implement the evolution of the qubits' state under a given Hamiltonian, acting on all qubits, which we call the *resource Hamiltonian*, of the form

$$\bar{H}_{\mathcal{C}} = \sum_{(j,k)\in\mathcal{C}} \bar{g}_{jk} Z^j Z^k . \tag{1}$$

The continuous evolution of all qubits under the resource Hamiltonian, for some tunable time t, is called an *analog block*:

$$U_{\bar{H}_{\mathcal{C}}}(t) = \exp\left(-i\, t \bar{H}_{\mathcal{C}}\right) . \tag{2}$$

The goal of DAQC is to, using only analog blocks and SQGs, effectively engineer the evolution under a different Hamiltonian, which we call the *target Hamiltonian*, of the form

$$H_{\mathcal{C}} = \sum_{(j,k)\in\mathcal{C}} g_{jk} Z^j Z^k . \tag{3}$$

[4] Note that a digital–analog quantum circuit can be defined in different ways, i.e. any circuit in which digital and analog operations are utilized could be called digital–analog [8]. Additionally, different definitions of analog evolution may exist, like a continuous evolution comprising less than all the qubits of the device [10]. However, in this manuscript, we focus our attention on the method called 'Digital–Analog Quantum Computation' laid out in [1] and further utilized in [2–7]. This provides a universal compilation technique to execute any quantum computation, based on an analog evolution comprising all qubits combined with SQGs, by effectively implement an inhomogeneous Ising model Hamiltonian.

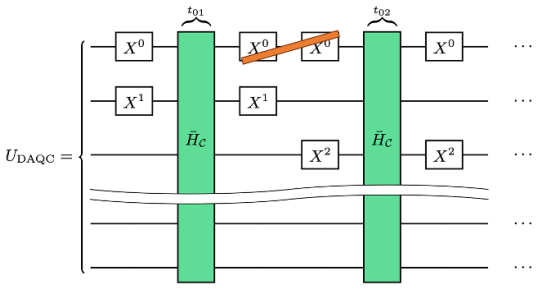

Figure 1. Digital–analog circuit consisting of c analog blocks. Each analog block runs for time t_{mn}, and is preceded and followed by the gates $X^m X^n$, for each pair of connected qubits $(m, n) \in \mathcal{C}$. More details on the construction of a DAQC circuit can be found in appendix A.

This can be done by constructing a quantum circuit that interleaves c analog blocks and specific sequences of SQGs, where c is the number of couplings of the device, as shown in figure 1. The sequences of SQG are, specifically, pairs of gates $X^m X^n$ executed before and after each analog block, for each pair of connected qubits $(m, n) \in \mathcal{C}$. Their purpose is to effectively change the sign of some of the coupling coefficients of the resource Hamiltonian (1) in each analog block (2). These positive and negative coefficients are combined by executing each analog block for the appropriate time, in order to effectively engineer an evolution under the target Hamiltonian (3). The time that each analog block in the quantum circuit must be executed for is calculated via the matrix equation

$$\mathbf{t} = M^{-1}\mathbf{G}t_f, \tag{4}$$

where $\mathbf{t}$ is the vector of times of the analog evolutions, with each element t_β being the time that the βth analog block must be executed for; M is a matrix whose elements are $M_{\alpha\beta} = +1\ (-1)$ if the effective coupling corresponding to the αth coupling, during the βth analog block, is positive (negative); $\mathbf{G}$ is a vector whose elements are $G_\beta = \frac{\bar{g}_\beta}{g_\beta}$, where $\bar{g}_\beta, g_\beta$ are the coefficients in equations (1) and (3) respectively; and t_f is the desired evolution time under the target Hamiltonian (3).

This construction of a digital–analog circuit requires the analog blocks to be 'turned on and off' sequentially to allow for the execution of layers of SQGs. However, there is an alternative paradigm called banged DAQC (bDAQC), which requires the analog interaction to be on throughout the whole quantum circuit, with SQGs being applied simultaneously to it. Given that, in general, the SQGs' Hamiltonians do not commute with that of the analog evolution, it introduces an error intrinsic to bDAQC in the computation. The reasoning is that this would be supposed to reduce the errors associated with 'turning the analog blocks on and off' [1]. More details on this paradigm can be found in appendix A.4.

In this manuscript, we set out to study the scaling of the errors in Ising DAQC as the size of the computation (i.e. the number of qubits) grows, and compare it to that of DQC. Additionally, we apply this analysis to two illustrative examples: the QFT routine and the GHZ state preparation, along with simulations of both.

3. Error scaling in DAQC

The DAQC method introduces errors that differ from those in DQC in several ways. In this section, we study how these errors scale with the number of couplings and of qubits of the device, and how they compare to the DQC paradigm.

We focus our analysis on the coherent errors related to imperfect control parameters, given that these are ubiquitous across quantum computing platforms, whereas the nature of incoherent environmental errors can vastly change across them. However, we make some general remarks on the latter in section 3.1.3.

3.1. Analog blocks

Even assuming that the implementation of analog evolution under the resource Hamiltonian (see equation (1)) yields two-qubit terms more accurate than those of TQGs, in this section we argue that the number of such two-qubit terms grows so quickly with the number of qubits that any possible advantage is quickly negated.

Performing a DAQC algorithm requires, as explained in section 2 and further detailed in appendix A, to construct a digital–analog quantum circuit with c analog blocks for each target Hamiltonian that needs to be implemented, where c is the total number of couplings. As an example, we provide the digital–analog circuit

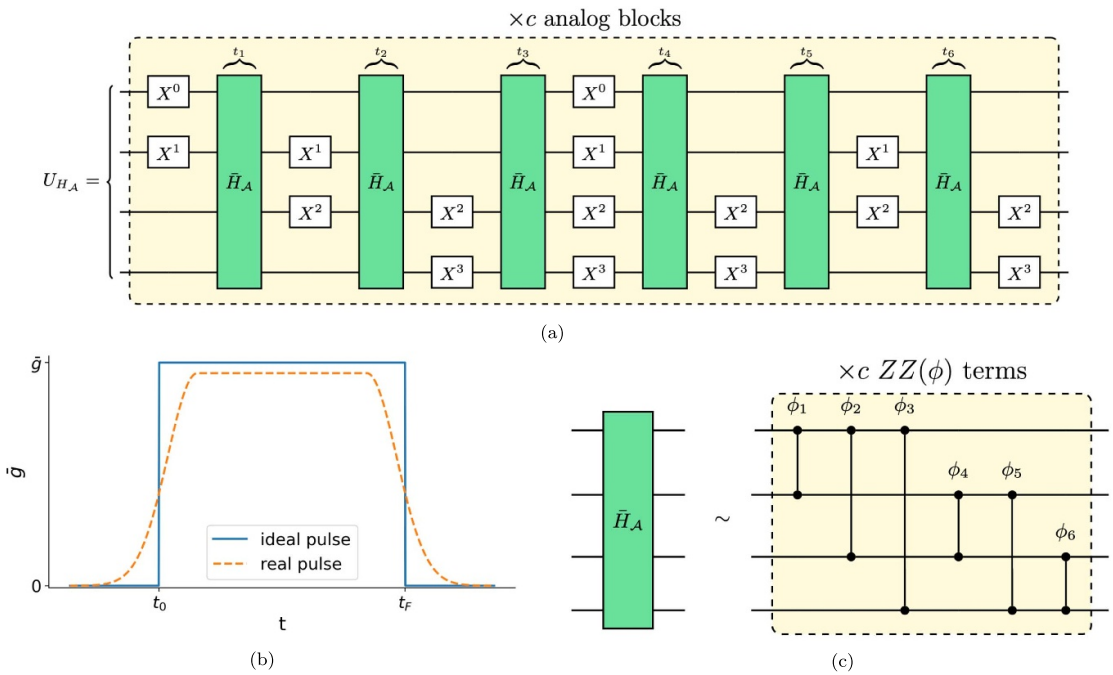

Figure 2. Schematic representation of error sources in a DAQC algorithm: (a) the number of analog blocks per implementation of a target Hamiltonian $H_{\mathcal{A}}$, for an ATA device with 4 qubits and resource Hamiltonian $\bar{H}_{\mathcal{A}}$, for which $c = 6$; (b) errors associated to each analog block, modeled as an uncertainty in the starting and finishing times of application t_0, t_F (ramp-up and ramp-down errors), and by an error in the coupling coefficients $\bar{g}$; (c) the number of two-qubit terms prone to mischaracterization present in an analog block, for an ATA device with 4 qubits and resource Hamiltonian $H_{\mathcal{A}}$.

for implementing a target Hamiltonian on a four-qubit device with ATA connectivity, for which $c = 6$, in figure 2(a).

3.1.1. Ramp-up and ramp-down errors

Calibration errors can be produced when switching on and off the analog blocks [11], a process during which the evolution differs from the ideal square pulse necessarily assumed in theory. Such errors can be modeled as an uncertainty in the time t of application of the resource Hamiltonian (see figure 2(b)). Additionally, the ramp-up and ramp-down procedure can introduce other types of error, such as leakage to non-computational states [12, 13].

These errors are particularly relevant within sDAQC, which requires ramping up and down the resource Hamiltonian's coupling coefficients repeatedly during the algorithm, whereas bDAQC mitigates this error by requiring it only at the beginning and end of the execution of the circuit.

3.1.2. Two-qubit terms in analog blocks

The resource Hamiltonian considered should be descriptive of the *natural* dynamics of the device. However, there might be several sources of characterization errors associated to their implementation:

- The resource Hamiltonian might still be an approximation to the actual dynamics for some quantum computing platforms. This is the case, for example, in superconducting qubit devices where the native dynamics are described with a Bose–Hubbard Hamiltonian [14], and the qubitized form of the Hamiltonian is still an approximation to it [15, 16]. In this case, a qubitized form of the Hamiltonian reduced to two-qubit interactions is in general valid only at relatively short times after the activation of an analog block. In appendix E, we study in detail how this is the case for superconducting qubits, where extra terms coupling pairs of qubits that are not directly coupled appear in the qubitized Hamiltonian, as well as other terms coupling three and more qubits. The coupling strength of these parasitic terms represents a significant fraction of the desired interaction strength, especially at larger desired coupling strengths.
- The parameters of the resource Hamiltonian might be inaccurately characterized. By definition, the resource Hamiltonian $\bar{H}_C$ contains c coupling coefficients, $\bar{g}_{jk}$. This means that the execution of each analog block introduces c terms that have a potential mischaracterization error, even assuming that the physical Hamiltonian will always have the exact form as in equation (1). Such an error can be modeled as an uncertainty in the coupling coefficients $\bar{g}$ of the resource Hamiltonian (see figure 2(b)).

As an example of the latter, we show the equivalence of one analog block as two-qubit ZZ terms,

$$ZZ(\phi) = \mathrm{e}^{i\phi Z^j Z^k} = \begin{pmatrix} \phi & 0 & 0 & 0 \\ 0 & -\phi & 0 & 0 \\ 0 & 0 & -\phi & 0 \\ 0 & 0 & 0 & \phi \end{pmatrix}, \tag{5}$$

on a four-qubit device with ATA connectivity in figure 2(c). In general, the calibration of a large number of digital gates is simpler compared to the calibration of an analog block of the same size, since we can calibrate each gate individually. In this regard, the precise many-body Hamiltonian identification needed for the successful characterization of an analog block is still the subject of ongoing research [14, 17–19].

We know that the implementation of a target Hamiltonian requires c analog blocks (figure 2(a)), and that each analog block introduces c two-qubit terms (figure 2(c)). Thus, the total number of two-qubit terms needed to implement a target Hamiltonian is c^2. As an example, for the ATA connectivity, for which $c = \Theta(N^2)$, the total number of error-prone two-qubit terms introduced is $\Theta(N^4)$ in the general case. On the other hand, implementing an equivalent computation in the DQC paradigm would require a minimum of $\Omega(1)$ and, in the worst case, $\mathcal{O}(N^2)$ TQGs, yielding a considerably slower scaling of the errors. Therefore, we conclude that Ising DAQC is unfavorable when compared to DQC for executing arbitrary quantum algorithms, which is where it should excel given that it is a universal paradigm for quantum computation.

In terms of fidelities, the fact that DAQC for the Ising model introduces c^2 two-qubit terms, as opposed to DQC introducing only c, implies that no matter how high the fidelity of a two-qubit term in DAQC is, it will inevitably underperform DQC beyond some finite (typically small) system size. This follows from the assumption that each error is independent [20], and therefore the contribution of all two-qubit terms to the total fidelity of the computation, F, is given by

$$F = f^n, \tag{6}$$

where f is the fidelity of each two-qubit term, and n is the number of such terms. By equating the fidelities of DAQC and DQC for the implementation of one target Hamiltonian,

$$f_{\mathrm{DAQC}}^{c^2} = f_{\mathrm{DQC}}^{c}, \tag{7}$$

assuming that $f_{\mathrm{DAQC}} > f_{\mathrm{DQC}}$, and solving for the critical number of connections c_c at which DAQC underperforms DQC, we obtain

$$c_{\mathrm{c}} = \frac{\log f_{\mathrm{DQC}}}{\log f_{\mathrm{DAQC}}}. \tag{8}$$

This means that, necessarily, the two fidelities cross at some device size for which $c = c_c$ even if $f_{\mathrm{DAQC}} \gg f_{\mathrm{DQC}}$. For the ATA connectivity case, where the number of connections scales as $c = N(N-1)/2$, solving for the critical number of qubits N_c at which DAQC underperforms DQC gives

$$N_{\mathrm{c}} = \frac{1 + \sqrt{1 + \frac{8 \log f_{\mathrm{DQC}}}{\log f_{\mathrm{DAQC}}}}}{2}. \tag{9}$$

To illustrate, even in the highly favorable case where two-qubit terms in an analog block have a fidelity of $f_{\mathrm{DAQC}} = 0.99$ and DQC TQGs have a much lower fidelity of $f_{\mathrm{DQC}} = 0.9$, DAQC for the Ising model would already underperform for systems as small as $N_c \geqslant 6$. This highlights that, despite potentially better fidelity per operation, DAQC's inherently worse scaling for the Ising model in the number of error-prone terms ensures that it will always lose to DQC beyond a modest system size. A more detailed discussion on the compound fidelity of DAQC compared to DQC can be found in section 3.5.

3.1.3. Environmental errors

As in the digital case, the dynamics of analog blocks are subject to the impact of its environment, which produces decoherence and information losses. While the environment responsible for the coherence decay is the same in both the digital and DAQC cases, the analog blocks may dissipate in a more complex and potentially faster way specifically at longer timescales, where the presence of non-local decaying channels involving multiple neighboring qubits may become increasingly relevant [21–24]. Depending on the physical implementation of the qubit states, many-body effects related to collective decay can arise in a variety of physical systems, such as e.g atom arrays [25, 26], quantum dots [27] and also in superconducting circuits [28, 29].

3.2. Depth and duration

The depth of a digital quantum circuit is defined as the number of distinct timesteps at which gates are applied [30]. It constitutes a measure of how long it takes to execute the quantum circuit, because each gate generally has a fixed duration.

In the DAQC framework, the number of distinct timesteps is not directly related to how long it takes to execute a quantum circuit, because each analog block in general has a different duration. Therefore, we need to sum the duration of the analog blocks and layers of SQGs. Recall that the vector of the analog block times is calculated via the matrix M^{-1} (see equation (4)), and no general statements can be made on the form of M^{-1}. Thus, the duration of DAQC algorithms must be calculated and studied on a case-by-case basis. In section 5, we calculate numerically the total runtime of the algorithms that we explore in this manuscript. In the previous literature, there is no quantitative study of the duration of DAQC circuits, and in fact, in section 5.2.1, we find contradictions with previous statements of DAQC circuits being faster than DQC circuits.

3.3. SQGs

The DAQC method introduces extra X gates to simulate one target Hamiltonian. From the method presented in [1] or, e.g from figure 2(a), it is straightforward to see that $\Theta(1)$ X gates are introduced per analog block. Thus, the number of extra SQGs introduced per target Hamiltonian is $\Theta(c)$.

3.4. bDAQC non-commutativity errors

As discussed in section 2, and in appendix A.4 in more detail, the bDAQC paradigm does not require to switch on and off the analog blocks repeatedly, but only requires the activation of a single block during the whole protocol, thus reducing the ramp-up and ramp-down errors. However, in bDAQC, the non-commutativity of SQGs with the resource Hamiltonian also introduces an error, which would only disappear for infinitely fast SQGs [1]. The non-commutativity error is different for the boundary analog blocks (the first and the last of the DAQC circuit) and the central analog blocks. In this section, we only focus on the central analog blocks because there are $\Theta(c)$ of them per target Hamiltonian, whereas there are only 2 boundary analog blocks per circuit.

Specifically, when a SQG generated by a Hamiltonian H_s^a applied for some time Δt, $U^a = \exp(-iH_s^a\Delta t)$, is applied on qubit a, the error introduced is given by [1]

$$e_{\text{central}} = \left\| 1 - \mathrm{e}^{-\mathrm{i}\bar{H}\Delta t/2}\mathrm{e}^{-\mathrm{i}H_s^a\Delta t}\mathrm{e}^{-\mathrm{i}\bar{H}\Delta t/2}\mathrm{e}^{\mathrm{i}(\bar{H}+H_s^a)\Delta t} \right\| \tag{10}$$

$$= \frac{(\Delta t)^3}{4} \left\| \left[[\bar{H}, H_s^a], \bar{H} + 2H_s^a \right] \right\| + \mathcal{O}\left((\Delta t)^4\right). \tag{11}$$

In the following, we work out the explicit dependence on Δt by carefully analyzing equation (11). If a SQG has a given rotation angle (for example, if it is a π-rotation around the X axis), the amplitude of its generator Hamiltonian is inversely proportional to the SQG's time: $H_s^a = \frac{\pi}{2\Delta t}X$. Since the Hamiltonian that generates the SQG, H_s^a, appears twice in the nested commutators of equation (11), we find that the explicit dependence of the error e_{central} on the SQG gate time Δt is linear, $e_{\text{central}} = \Theta(\Delta t)$. This result is in contradiction with previous literature [1, 4], where it is stated to have a significantly better scaling of $\mathcal{O}((\Delta t)^3)$.

Additionally, the resource Hamiltonian $\bar{H}$ also appears twice in the nested commutators. Thus, there is an additional dependence with the degree of qubit a (i.e. the number of couplings) and with the resource Hamiltonian's coupling coefficients.

Specifically, the infidelity introduced by the non-commutativity of a gate X^a with the resource Hamiltonian $\bar{H}$ is

$$\epsilon_{\text{central}} = \Theta\left(d_a\bar{g}\Delta t + d_a^2\bar{g}^2\Delta t^2\right), \tag{12}$$

where d_a is the degree of qubit a, and $\bar{g}$ is the coupling coefficient of the resource Hamiltonian (assumed to be homogeneous for simplicity). A detailed derivation of the scaling given in equation (12) is provided in appendix F.

3.5. Compound fidelity

In this subsection, we aim to write approximate formulas for the fidelities of DQC, sDAQC and bDAQC that account for the scaling of all the sources of error studied in this section, and their individual infidelity contributions. In order to do so, we make two assumptions:

1. Each one- and two-qubit term in an evolution operator U corresponding to a SQG, TQG or analog block has a fidelity $f < 1$ arising from control errors, which is independent of all other operations [20].
2. The main source of decoherence is thermal relaxation, and we consider a simple Markovian model for it, such that the fidelity per qubit for an algorithm that requires a time t has the approximate form $F_{T_1} \approx \mathrm{e}^{-t/T_1}$, where T_1 is the relaxation time. Additionally, we consider this infidelity to be independent for each qubit, and also independent from their unitary dynamics (disregarding the complex decaying channels that can arise in DAQC, as discussed in section 3.1.3).

Under these assumptions, the approximate total fidelity of a digital circuit implementing one given target Hamiltonian with $\mathcal{O}(c)$ terms on a device with c couplings is

$$F_{\mathrm{DQC}} \approx \left(f_{\mathrm{TQG}}\right)^{n_{\mathrm{TQT}}} \times e^{-Nt_{\mathrm{tot}}/T_1} \tag{13}$$

$$= \left(f_{\mathrm{TQG}}\right)^{\mathcal{O}(c)} \times e^{-Nt_{\mathrm{tot}}/T_1}, \tag{14}$$

where f_{TQG} is the fidelity of each TQG, n_{TQT} is the number of two-qubit terms (i.e. of TQGs) and t_{tot} is the total execution time of the circuit. The compound fidelity F_{DQC} in equation (14) accounts for that of the TQGs, and decoherence due to thermal relaxation.

On the other hand, the approximate fidelity of a stepwise digital–analog circuit implementing the same target Hamiltonian is given by

$$F_{\mathrm{sDAQC}} \approx \left[\left(f_{\mathrm{ramp}}\right) \times \left(f_{\mathrm{coupling}}\right)\right]^{n_{\mathrm{TQT}}} \times \left(f_{\mathrm{SQG}}\right)^{n_{\mathrm{SQG}}} \times e^{-Nt_{\mathrm{tot}}/T_1}, \tag{15}$$

$$= \left[\left(f_{\mathrm{ramp}}\right) \times \left(f_{\mathrm{coupling}}\right)\right]^{c^2} \times \left(f_{\mathrm{SQG}}\right)^{\Theta(c)} \times e^{-Nt_{\mathrm{tot}}/T_1}, \tag{16}$$

where f_{ramp} is the fidelity associated with the ramp-up and ramp-down errors, f_{coupling} is the fidelity associated with the mischaracterization of $\bar{g}$, f_{SQG} is the fidelity of SQGs, and n_{SQG} is the number of SQGs.

Finally, the approximate fidelity of a banged digital–analog circuit implementing said target Hamiltonian is

$$F_{\mathrm{bDAQC}} \approx \left[\left(f_{\mathrm{ramp}}\right)^{c} \times \left(f_{\mathrm{coupling}}\right)^{n_{\mathrm{TQT}}}\right] \times \left(f_{\mathrm{SQG}}\right)^{n_{\mathrm{SQG}}} \times e^{-Nt_{\mathrm{tot}}/T_1} \times \left(1-\epsilon_{\mathrm{central}}\right)^{n_{\mathrm{AB}}}. \tag{17}$$

$$= \left[\left(f_{\mathrm{ramp}}\right)^{c} \times \left(f_{\mathrm{coupling}}\right)^{c^2}\right] \times \left(f_{\mathrm{SQG}}\right)^{\Theta(c)} \times e^{-Nt_{\mathrm{tot}}/T_1} \times \left(1-\epsilon_{\mathrm{central}}\right)^{c}, \tag{18}$$

where n_{AB} is the number of analog blocks. In this case, the contribution to infidelity from ramp-up and ramp-down errors gets significantly reduced, while the infidelity from non-commutativity is introduced.

As discussed in section 3.1.2, the dominant factor in determining the overall fidelity is the scaling of the number of error sources. A faster-growing accumulation of errors in one paradigm ensures that it will eventually underperform the others, typically at a small system size, regardless of the single-operation fidelity f.

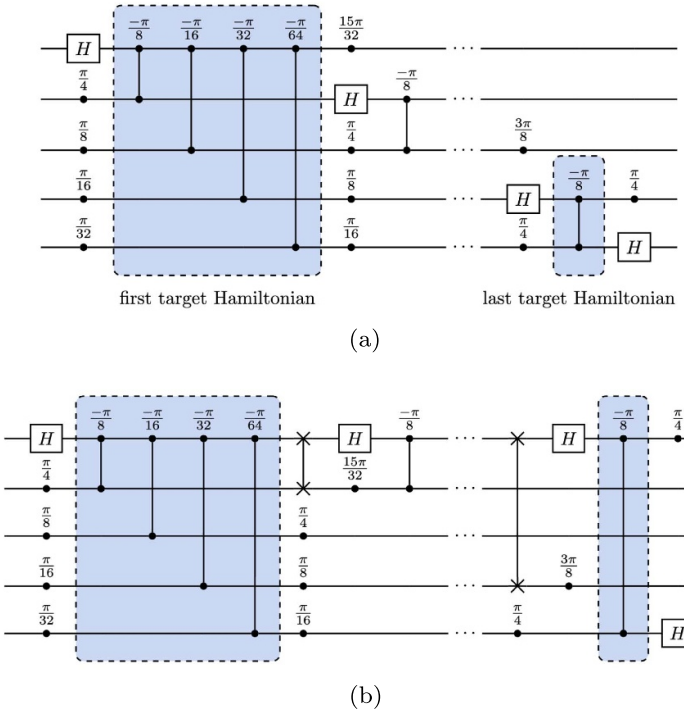

Figure 3. Digital circuit for the QFT on a device with five qubits, comprising H, $R_z(\theta)$ and $ZZ(\phi)$ gates, (a) on an ATA connectivity, and (b) on a star-connectivity, where SWAP gates have been introduced as necessary. Target Hamiltonians as required by DAQC are highlighted.

4. Illustrative examples: QFT and GHZ state generation

In this section, we apply the analysis above to two algorithms: the QFT routine and the GHZ state generation. We have chosen QFT as a representative example because it has been said in the literature to provide an advantage when compared to DQC [4, 5], which we here disprove, exemplifying our claim that DAQC is ineffective for executing arbitrary algorithms. On the other hand, we have chosen the GHZ state preparation as an example of the extremely specific circumstances under which DAQC can actually provide an advantage. We confirm our findings with simulations in section 5.

4.1. QFT

The QFT is a quantum routine that acts on a quantum state $|x\rangle = \sum_{i=0}^{2^N-1} x_i |i\rangle$, where $|i\rangle$ are computational basis states, and maps it to a Fourier-transformed quantum state $\sum_{i=0}^{2^N-1} y_i |i\rangle$, with

$$y_k = \frac{1}{\sqrt{N}} \sum_{j=0}^{N-1} x_j \omega_N^{jk}, \quad k = 0, 1, 2, 3 \ldots, N-1, \tag{19}$$

where $\omega_N = e^{2\pi i/N}$. A digital quantum circuit for this routine is depicted in figure 3(a) using the Hadamard (H), and phase $R_z(\theta)$ SQGs,

$$H = \frac{1}{\sqrt{2}} \begin{pmatrix} 1 & 1 \\ 1 & -1 \end{pmatrix}, \tag{20}$$

$$R_z(\theta) = e^{-i\frac{\theta}{2}Z} = \begin{pmatrix} 1 & 0 \\ 0 & e^{i\theta} \end{pmatrix}, \tag{21}$$

as well as the $ZZ(\phi)$ TQG (5).

4.1.1. ATA QFT

Following the analysis in section 3, we study the scaling of errors for the digital–analog QFT routine in an ATA connectivity device, and compare them to those of a purely digital implementation, in table 1(a). The step-by-step derivation of these scalings can be found in appendix G.1. The most notable is that of the

Table 1. Scaling of the error sources in DQC and DAQC with the number of qubits N, from which the total fidelity of the quantum circuit can be calculated using equations (13), (15) and (17) for DQC, sDAQC and bDAQC respectively, for the following algorithms: (a) QFT on an ATA connectivity, for which all sources of error scale better in DQC than in DAQC; (b) QFT on a star-connectivity, for which the sources of error in DAQC scale better than in the ATA case, with an advantage with respect to DQC in the time of execution; and (c) GHZ state preparation on a star-connectivity, for which we do not consider bDAQC (and therefore also not its associated error $\epsilon_{\text{central}}$) given that it contains only one analog block, and all the sources of error in DAQC scale similarly or better than those in DQC.

(a) ATA-QFT

	n_{AB}	n_{TQT}	n_{SQG}	t	$\epsilon_{\text{central}}$
DQC	—	$\mathcal{O}(N^2)$	$\mathcal{O}(N)$	$\mathcal{O}(N)$	—
sDAQC	$\mathcal{O}(N^3)$	$\mathcal{O}(N^5)$	$\mathcal{O}(N^3)$	$\mathcal{O}(N^{2.05})$	—
bDAQC	$\mathcal{O}(N^3)$	$\mathcal{O}(N^5)$	$\mathcal{O}(N^3)$	$\mathcal{O}(N^{2.05})$	$\mathcal{O}(N^2)$

(b) Star-QFT

	n_{AB}	n_{TQT}	n_{SQG}	t	$\epsilon_{\text{central}}$
DQC	—	$\mathcal{O}(N^2)$	$\mathcal{O}(N)$	$\mathcal{O}(N^2)$	—
sDAQC	$\mathcal{O}(N^2)$	$\mathcal{O}(N^3)$	$\mathcal{O}(N^2)$	$\mathcal{O}(N)$	—
bDAQC	$\mathcal{O}(N^2)$	$\mathcal{O}(N^3)$	$\mathcal{O}(N^2)$	$\mathcal{O}(N)$	$\mathcal{O}(1)$

(c) Star-GHZ

	n_{AB}	n_{TQT}	n_{SQG}	t
DQC	—	$\mathcal{O}(N)$	$\mathcal{O}(N)$	$\mathcal{O}(N)$
sDAQC	1	$\mathcal{O}(N)$	$\mathcal{O}(N)$	$\mathcal{O}(1)$

number of two-qubit terms, which is $\Theta(N^2)$ for the digital case while it is $\Theta(N^5)$ for the digital–analog case, rendering the DAQC implementation of the algorithm extremely unfavorable.

This result directly contradicts claims made in [4] that 'the fidelity of the DQC decreases faster than the fidelity of the DAQC [QFT] with the number of qubits of the system'. This is only apparently the case from the data in [4] because:

1. The parameters used in the simulations are extremely favorable for DAQC: the fidelity of the TQGs is chosen to be $f_{\text{TQG}} = 98.1\%$, while a two-qubit analog block equivalent to that gate has $f_{\text{analog}} = 99.96\%$. These fidelities have been calculated using the error parameters provided in [4] and averaging over 10 000 noisy operations,
2. The simulations in [4] reach only up to seven qubits, right before DQC would significantly outperform DAQC at 8 qubits or more. This evidences that, even for parameters that are very favorable to DAQC, DQC quickly outperforms it due to its fundamentally better scaling.

Regarding the duration of the quantum circuits, the fact that it scales significantly worse in DAQC (approximately quadratically with N) than in DQC (linear with N) also directly contradicts the claim made in [4] that the authors 'have shown that the DAQC paradigm can enhance the depth of the implementation of a quantum algorithm [QFT].'

Finally, we predict that bDAQC provides no advantage with respect to sDAQC, given that the intrinsic error introduced scales too quickly (see the contribution of this source of error to the total fidelity in equation (18)).

This unfavorable scaling of the errors in digital–analog QFT also affect the digital–analog implementations described for the Quantum Phase Estimation [5] and Harrow-Hassidim-Lloyd [6] algorithms, given that both use QFT as a subroutine.

4.1.2. Star QFT

We have developed a DAQC protocol that is specifically tailored to a device with star connectivity, where one qubit is directly coupled to many others. This protocol, which we describe in detail in appendix H, is optimal in terms of the number of analog blocks required and their durations, potentially providing significant improvements when compared to the ATA connectivity. In this subsection, we discuss the scaling of errors of the implementation of digital–analog QFT applied on such a device using this optimal protocol (see figure 3(b) for the digital quantum circuit of this algorithm). Similarly to the case of ATA-QFT, a summary of the error scalings of star-QFT can be found in table 1(b) whereas a step-by-step derivation can be found in appendix G.2.

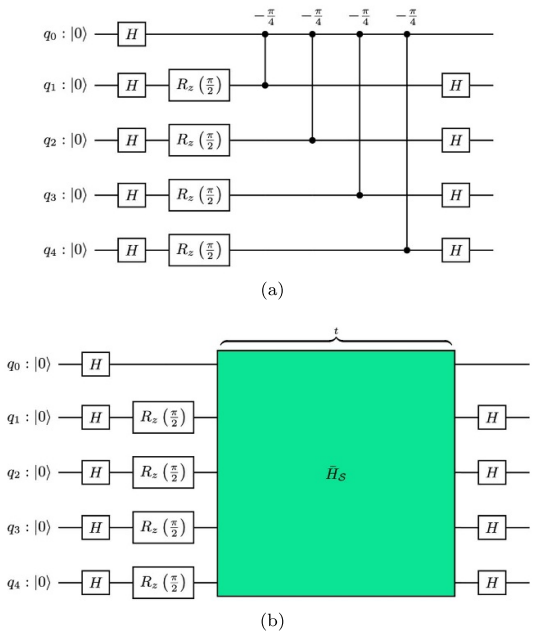

Figure 4. Quantum circuits implementing the GHZ state preparation protocol on a star-connectivity with five qubits: (a) in the DQC paradigm, (b) in the sDAQC paradigm.

As expected, the errors for star-QFT scale slower when compared to the ATA-QFT. However, the scaling is generally still worse than in DQC. In detail, the number of two-qubit terms is $\Theta(N^2)$ in the digital case and $\Theta(N^3)$ in the digital–analog one.

In this case, the duration of the algorithm scales linearly in DAQC while it scales quadratically in DQC, so it presents an advantage in that regard. Additionally, the intrinsic error introduced by bDAQC is smaller than that introduced by the two-qubit terms, so bDAQC has the potential of outperforming sDAQC.

4.2. GHZ state preparation

In this subsection, we introduce another example of a digital–analog quantum algorithm and describe the DAQC protocol for generating the maximally entangled Greenberger–Horne–Zeilinger (GHZ) state [31] in a star-connectivity device with N qubits,

$$|\mathrm{GHZ}_N\rangle = \frac{|0\rangle^{\otimes N} + |1\rangle^{\otimes N}}{\sqrt{2}}. \tag{22}$$

In figure 4(a), we show the digital circuit for generating the GHZ state on $N = 5$ qubits by utilizing $ZZ(-\frac{\pi}{4})$ gates. We can write the $N-1$ consecutive ZZ gates appearing in the digital circuit as the evolution operator

$$U = \mathrm{e}^{-\mathrm{i}\sum_{j=1}^{N} \frac{\pi}{4} Z^0 Z^j}, \tag{23}$$

where we have set the time of the evolution $t_f = \frac{\pi}{4g}$. Writing a digital–analog circuit for this algorithm is now possible following the method described in appendix H.

In this section we assume the resource Hamiltonian is homogeneous, i.e. all its coupling coefficients $\bar{g} \equiv \bar{g}_{0j}$ are equal, and also that they are independent of the number of qubits N. This entails that the digital–analog quantum circuit only requires one analog block with appropriate runtime (see figure 4(b)), which is given by the relation between the coefficients of the target and the resource Hamiltonians, $t = g/\bar{g}$. This runtime t is independent of the number of qubits, whereas the number of TQGs needed in the digital paradigm, and thus also the runtime of the algorithm, scales linearly with the number of qubits. A comparison of the scaling of the digital–analog and the purely digital implementations of this algorithm can be found in table 1(c). In this case, we do not consider bDAQC (and therefore also not its associated error $\epsilon_{\mathrm{central}}$), because only one analog block is present and thus bDAQC presents no advantage.

For this algorithm, we can see that DAQC scales similarly to the DQC paradigm for two-qubit terms, and better for execution time. This is because, in this case, the target and resource Hamiltonians are related just by a multiplicative factor, and thus just one analog block is required to simulate the target Hamiltonian.

Therefore, we argue that the cases in which $\Theta(1)$ analog blocks are required to execute $\Theta(c)$ two-qubit terms are the ones in which digital–analog circuits excel. However, such cases do not require the universal DAQC compilation method at all.

5. Numerical simulations

After studying the scaling of the sources of error of the three algorithms in section 4, we validate our findings through numerical simulations under a certain error model for different numbers of qubits, and extract average execution fidelities as well as durations of circuit execution.

5.1. Error model and methods

DQC employs single- and TQGs, whereas DAQC employs SQGs and analog blocks. As discussed in section 3, we model the errors caused by all these operations by introducing errors in their control parameters. We introduce a coherent and an incoherent contribution of these control errors to the total infidelity by implementing two different modifications to the control parameters: (1) systematic errors that are constant throughout each noisy simulation of the quantum circuit and (2) stochastic errors that are randomly chosen every time an operation gets applied.

For each SQG generated by a Hamiltonian H_s^a, $U_{H_s^a}(\theta) = \exp(-i\theta H_s^a)$, we modify the angle of the rotation as

$$\theta \to \theta' = \theta \times (1 + \Delta\theta + \delta\theta)\,, \tag{24}$$

where $\Delta\theta$ is the *systematic* error, and $\delta\theta$ is the *stochastic* error.

For each TQG, $ZZ(\phi) = \exp(-i\phi Z^j Z^k)$, we modify the phase of the rotation as

$$\phi \to \phi' = \phi \times (1 + \Delta\phi + \delta\phi)\,, \tag{25}$$

where $\Delta\phi$ is the systematic error, and $\delta\phi$ is the stochastic error.

Finally, for each analog block, $U_{\bar{H}_c}(t) = \exp(-it\sum \bar{g}_{jk} Z^j Z^k)$, we modify the runtime and coupling coefficients of the resource Hamiltonian as

$$t \to t' = t \times (1 + \Delta t + \delta t)\,, \tag{26}$$

$$\bar{g} \to \bar{g}' = \bar{g} \times (1 + \Delta\bar{g} + \delta\bar{g})\,, \tag{27}$$

where $\Delta t, \Delta\bar{g}$ (systematic), and $\delta t, \delta\bar{g}$ (stochastic) are unitless.

For the case of QFT, because we are interested in the fidelity of the process regardless of the initial state, we compute the ideal unitary implemented by the quantum circuit, and average over the erroneous unitaries' fidelities. We define the fidelity of one erroneous unitary U with respect to its ideal $\tilde{U}$ as its average fidelity over all possible initial states [32],

$$F_U = \frac{n + \left|\mathrm{Tr}\left(\tilde{U}^\dagger U\right)\right|^2}{n(n+1)}\,, \tag{28}$$

where $n = 2^N$ is the dimensionality of the Hilbert space.

On the other hand, for the case of the GHZ state preparation, because we are interested in the final state only, we compute the ideal state and average over the erroneous states' fidelities. We define the fidelity of one erroneous final state $|\psi\rangle$ with respect to its ideal state (22) as:

$$F_\psi = |\langle\psi|\mathrm{GHZ}_N\rangle|^2\,. \tag{29}$$

For the sake of specificity, we choose the error parameters of the simulations to match those of a state-of-the-art superconducting QPU. We sample all errors from a Gaussian distribution $\mathcal{N}(\mu = 0, \sigma^2)$ centered around 0, where σ^2 is chosen so that each type of operation has a given average fidelity: 99.99% for SQGs, 99.9% for TQGs, and 99.95% for each two qubit term in analog blocks. These figures are calculated executing the erroneous gates 10000 times, and averaging the resulting erroneous unitaries' fidelities according to equation (28).

This choice for the fidelities of each operation entails considerably better SQGs than TQGs, and analog blocks that introduce less error per two-qubit term than each TQG. Additionally, in the case of bDAQC, the error associated with the runtimes is applied only in the first and last analog blocks of the quantum circuit

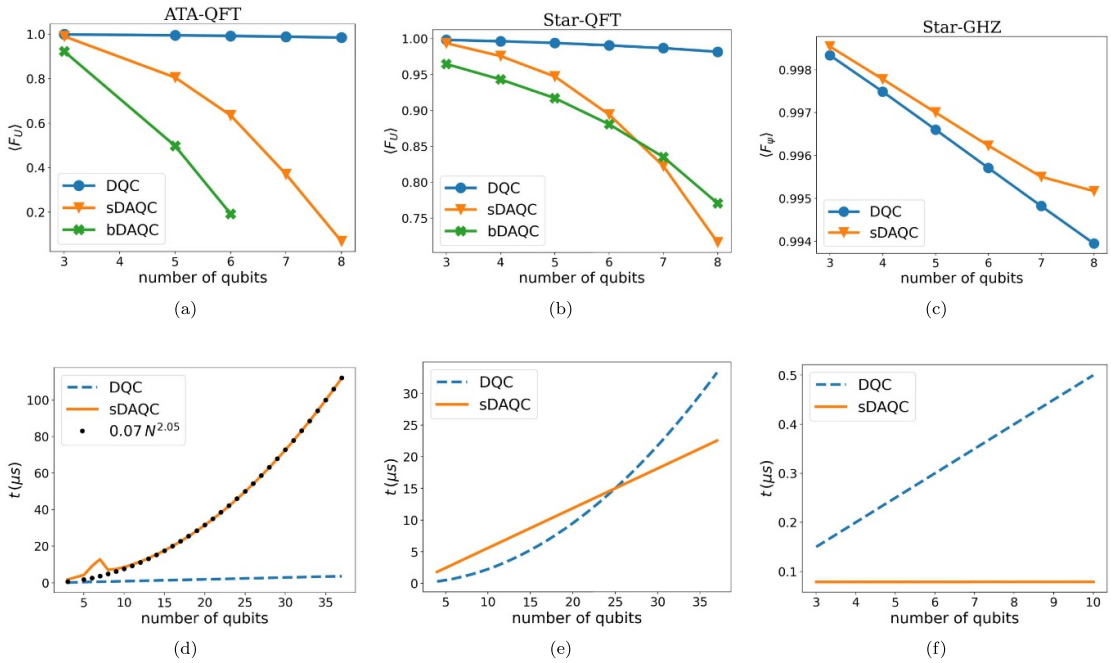

Figure 5. Top row: fidelity of DQC, sDAQC and bDAQC algorithms as a function of the number of qubits for the following algorithms: (a) ATA-QFT, for which both versions of DAQC perform worse than DQC; (b) star-QFT, for which both versions of DAQC perform worse than DQC, but bDAQC performs better than sDAQC for $N > 6$; and (c) star-GHZ, for which sDAQC performs better than DQC. **Bottom row**: duration of the DQC and sDAQC circuits of algorithms, calculated numerically by summing all the times of each SQG layer $\Delta t = 5$ ns and the elements of the vector of runtimes $\mathbf{t}$ (DAQC), and by summing the times of each TQG layer $t_{\mathrm{TQG}} = 50$ ns and SQG layer (DQC), as a function of the number of qubits: (d) ATA-QFT, for which we have fit the data to the closest signomial expression, $\mathcal{O}(N^{2.05})$, and the DAQC algorithm's execution is longer than DQC for the whole range; (e) star-QFT, for which the DQC algorithm's execution is longer than DAQC for $N > 25$; and (f) star-GHZ, for which the DQC algorithm's execution always is longer than DAQC.

(see section 3.1.1). Finally, all the values of σ are also chosen so that the coherent errors account for 25% of the infidelity per operation, and incoherent errors account for 75% of it.

We simulate the circuits for digital and digital–analog ATA-QFT, star-QFT and Star-GHZ, and compute the noisy fidelities for each case, after applying the errors described above. We do this by running 1000 iterations of noisy circuits, computing the resulting erroneous unitaries and final states according to equations (28) and (29), respectively, and averaging to obtain $\langle F_U \rangle$ in the case of QFT or $\langle F_\psi \rangle$ in the case of the GHZ state preparation.

The quantum circuits must be compiled to a specific basis gate set, which may be different for each quantum computing platform. For specificity, we focus our simulations on one consisting of superconducting qubits. Therefore, the native SQGs that we assume can be implemented in the devices are the R_z gate (21) and the R_{xy} gate,

$$R^a_{xy}(\theta,\phi) = \mathrm{e}^{-\mathrm{i}\frac{\theta}{2}(\cos\phi X^a + \sin\phi Y^a)}. \tag{30}$$

For superconducting quantum computers, the $R^a_{xy}(\theta,\phi)$ gate can be physically implemented via a microwave drive [33]. The gate $R^a_z(\theta)$ does not need to be physically implemented because it can be accounted for virtually by readjusting the phase of the subsequent gates applied on qubit a [34]. On the other hand, the native TQG we assume is the $ZZ^{jk}(\phi)$ gate (5).

We set the resource Hamiltonians to be homogeneous, with coupling coefficient $\bar{g} = 10$ MHz, and the SQG times to be $\Delta t = 5$ ns. On the other hand, we assume that the time it takes to implement a TQG does not depend on the phase of its rotation, and it is $t_{\mathrm{TQG}} = 50$ ns, as is realistic for superconducting transmon qubits coupled via tuneable couplers.

5.2. Results

Considering the error model and methods prepresented, we have performed our simulations using the open-source quantum computing library Qiskit [35] and the results are presented in figure 5.

In the top row of figure 5, we plot the fidelity of the digital and digital–analog computations for each algorithm we have studied (ATA-QFT[5], star-QFT and Star-GHZ), as a function of the number of qubits.

Likewise, in the bottom row of figure 5, we plot the times of execution of the quantum circuits as a function of the number of qubits. For the case of DAQC, these are calculated numerically by summing all the elements of the vector of analog runtimes, $\mathbf{t}$ resulting from equation (4), and the times of the SQG layers. On the other hand, for the case of DQC, they are calculated numerically by summing the times of SQG layers and of TQG layers. SQG and TQG times are those laid out in section 5.1; respectively, $\Delta t = 5\,\text{ns}$ and $t_{\text{TQG}} = 50\,\text{ns}$. Because we do not need to actually simulate the quantum circuits, we can extend these figures to a higher number of qubits. The times of bDAQC circuits are not represented because they overlap those of sDAQC.

We proceed to discuss these results in detail for each algorithm.

5.2.1. ATA QFT

As can be seen from figure 5(a), the fidelities of QFT in both DAQC paradigms are below the fidelity in DQC over the entire range of the number of qubits N studied. One reason is that, even though each two-qubit term in analog blocks is more error-robust, the number of two-qubit terms is much bigger than in DQC (recall the scalings in section 4.1.1). For example, in the case of $N = 3$, DQC has 3 two-qubit terms whereas DAQC has 18 of them. Additionally, in DAQC, the two-qubit terms are repeatedly applied on the same pairs of qubits, leading to a higher accumulation of coherent errors throughout the computation [36]. The much worse scaling of DAQC compared to DQC only exacerbates the difference in fidelity for a bigger number of qubits. This is expected from the estimation of compound fidelity (equations (14), (16) and (18)), as all factors (the number of analog blocks, the number of two-qubit terms and the number of SQGs) have a worse scaling in the DAQC paradigms, and bDAQC introduces a significant extra error compared to sDAQC. As discussed in section 3.1.2, the worse scaling of all error sources in the DAQC paradigms guarantees that it underperforms DQC in terms of overall execution fidelity, regardless of the fidelities of individual operations being higher.

Regarding the time of the computation, plotted in figure 5(d), we have fit the data to the best signomial expression[6], which gives a scaling of $\Theta(N^{2.05})$, whereas the computation time for DQC scales linearly as expected. The detrimental impact of decoherence is therefore much larger for DAQC than for DQC.

5.2.2. Star QFT

From figure 5(b), one can see that the fidelities for DAQC are also below the DQC fidelity for the whole range of N studied in this case. However, the fidelities of DAQC are higher with respect to the ATA case, as was expected from the analysis of the error scaling in appendix G.2. Thus, we see explicitly the dependence of the performance of DAQC on the connectivity and the compilation used for the digital–analog circuit. This result is in accordance with our estimations for the compound fidelity (equations (14), (16) and (18)), given that, similarly to the case of the ATA-QFT, all factors still scale better in DQC than in DAQC. Additionally, in this case, the intrinsic error associated with bDAQC scales slower than the error associated with the analog blocks (see table 1(c)), so the trade-off is favorable to bDAQC and it outperforms sDAQC for $N > 6$.

As for the time of computation, in figure 5(e), we see that for DAQC, it grows linearly, while for DQC, it grows quadratically, in such a way that for $N > 25$, the duration of the digital algorithm surpasses that of the digital–analog, as predicted in section 4.1.2. This is because, in DQC, the application of TQGs must be sequential since all of them involve the central qubit.

In this case, while the infidelity coming from control errors is greater for DAQC, there may be a trade-off with the infidelity arising from decoherence and other environmental noise related to the time of execution of the quantum circuits, which is greater for DQC than for DAQC for a big enough number of qubits. The total fidelity under both sources of noise is calculated approximately in appendix J, where we conclude that the trade-off can be favorable for DAQC for certain ranges of parameters, for example, if the execution of TQGs is extremely slow, and/or if the relaxation time T_1 of the qubits is extremely short.

[5] For ATA-QFT, we skip the case of $N = 4$. This is because, as explained in [1], the matrix M that results for the ATA connectivity with $N = 4$ is not invertible, and thus the times of the analog blocks cannot be calculated via equation (4). Furthermore, also for ATA-QFT, we simulate the bDAQC circuit only for 3, 5 and 6 qubits as those are the only cases in which the compilation described in [1] can be applied. For any $N > 6$, equation (4) may return negative runtimes for the analog blocks. Indeed, the ATA-QFT needs the implementation of analog blocks with negative runtimes, which is not physical. A protocol for obtaining a digital–analog circuit with only non-negative runtimes is given in [2], though it requires the construction of an M matrix whose size grows exponentially with the number of qubits, thus rendering it impractical.

[6] Additionally, a spike is present in the range $N \in (5, 8)$. This non-monotonic behavior is due to a property of the matrix M for the ATA connectivity: usually, its inverse M^{-1} has a balance of positive and negative elements that makes it so the contributions to analog times are partially cancelled in equation (4); however, for $N = 6, 7$ in the ATA connectivity, its elements are all negative and positive, respectively.

5.2.3. Star GHZ state preparation

In figure 5(c), we can see that the fidelities of sDAQC are better than those of DQC. This result agrees with our prediction regarding the fidelities of DQC (14) and sDAQC (16) made in section 4.2, given that the number of two-qubit terms is the same in both cases and the analog evolution is, by construction, more resilient to the control errors.

Additionally, and as expected, the time of the digital–analog algorithm is constant whereas that of the digital algorithm scales linearly with N (see figure 5(f)). This is because, in a way, the digital–analog algorithm is parallelizing all the two-qubit terms while the digital algorithm requires that we apply them sequentially, one after the other.

Therefore, DAQC presents an advantage with respect to DQC when we can express the evolution of many consecutive TQGs in a digital algorithm as a very reduced number of analog blocks, and combining them with SQGs, i.e. in the few cases in which the resource Hamiltonian is similar to the target Hamiltonian.

6. Conclusions

In the past few years, the DAQC paradigm has been presented as an alternative path to perform universal quantum computation that combines the robustness of analog quantum computing with the flexibility of the digital approach [1–7].

In this manuscript we have benchmarked its performance by analyzing, both analytically and numerically, the scaling of errors with respect to the digital case. Furthermore, we have considered the most general situation, i.e. regardless of the connectivity or the algorithm to be implemented. Our analysis shows a clearly disadvantageous error scaling of DAQC for the Ising model with respect to the digital case, primarily due to the number of analog blocks needed to engineer one target Hamiltonian, and the number of two-qubit terms introduced per each analog block. While for DAQC the implementation of one target Hamiltonian entails the introduction of c^2 two-qubit terms (where c is the number of couplings of the device), for DQC it only entails, at most, the introduction of c two-qubit terms.

To illustrate our scaling analysis, we have analyzed the performance of DAQC with respect to the digital case for two different algorithms, the QFT and the GHZ state preparation algorithm, on two different connectivities: ATA and a star configuration. We have consistently found DAQC to be less efficient in terms of fidelities when implementing two-body Ising Hamiltonians, except for the case in which the device's resource Hamiltonian closely matches the algorithm's target Hamiltonian. In this situation, it can be argued that the resulting quantum circuit corresponds to a purely analog implementation, with SQGs applied before and after the analog evolution (see, e.g figure 4(b)). While this implies the need for tailoring the device's connectivity to match that of the algorithm, this case shows a promising advantage as it parallelizes the two-qubit interactions that would otherwise be applied sequentially in the digital paradigm, and takes full advantage of the potentially more error-resilient analog evolution. This approach, however, does not require the DAQC universal compilation technique at all. Thus, we foresee potential areas of application of digital–analog techniques in quantum simulation [2, 8, 37–43] and variational algorithms in which fast generation of entanglement across the whole device is desirable [37, 44–46]. For 'generic' algorithms, where DAQC should excel given its universality, we have shown that it is unfavorable, fundamentally contradicting claims of DAQC improving the errors of quantum computations from the previous literature [4, 5]. Therefore, future work should be focused on either the potential areas of applicability of DAQC mentioned above, or on the specific case of quantum algorithms running on devices whose respective target and resource Hamiltonians share a structure that allows for a significant reduction of the errors introduced.

Data availability statement

The data cannot be made publicly available upon publication because no suitable repository exists for hosting data in this field of study. The data that support the findings of this study are available upon reasonable request from the authors.

Acknowledgments

We would like to acknowledge the support of our colleagues in IQM, and specially thank T Liu and B G Taketani. We also thank M Sanz for fruitful discussions at the early stages of our work, as well as P García-Molina. Finally, we acknowledge the support from the German Federal Ministry of Education and Research (BMBF) under DAQC (Grant No. 13N15686) and Q-Exa (Grant No. 13N16062).

Appendix A. Digital–analog quantum computation (DAQC) with arbitrary connectivity

Currently existing DAQC algorithms which can be implemented using two-body Ising Hamiltonians have been developed for an ATA qubit connectivity [1, 2, 4, 5, 7] and for a one-dimensional qubit chain with nearest neighbor couplings [2, 3]. However, promising quantum computing architectures like those based on superconducting qubits consist of planar devices where only local interactions with nearest neighbors can be natively implemented. In this section we provide a generalization by developing a protocol for implementing universal DAQC on a device with an arbitrary connectivity. A more succinct method to achieve such a general protocol is described in [2], which utilizes the ATA case as a starting point. For the sake of completeness, in this section we describe our method from the ground up.

A.1. Resource and target Hamiltonian

Throughout this manuscript, we distinguish between resource and target Hamiltonians:

- The *resource Hamiltonian* is the entangling Hamiltonian according to which the qubits of a device evolve naturally, when all interactions are turned on [1]. Its coupling coefficients are assumed to be constant and non-tunable during the computation, though they can be turned on or off simultaneously as desired. In the following, we denote resource Hamiltonians as $\bar{H}$.
- The *target Hamiltonian* is the entangling Hamiltonian that generates a specific unitary which we wish to implement. Its coupling coefficients can be chosen arbitrarily, depending on the computation to be implemented. We denote target Hamiltonians as H.

We assume that the resource Hamiltonians are of ZZ-Ising type and that the target Hamiltonians that we wish to implement are also of the ZZ-Ising type,

$$\bar{H}_{\mathcal{C}} = \sum_{(j,k)\in\mathcal{C}} \bar{g}_{jk} Z^j Z^k , \tag{A1}$$

$$H_{\mathcal{C}} = \sum_{(j,k)\in\mathcal{C}} g_{jk} Z^j Z^k , \tag{A2}$$

where, formally, we have defined the connectivity of a device (i.e. that of its resource Hamiltonian) as the collection of c pairs of qubits that are connected, and we write it as $\mathcal{C} = \{(j,k)\}$, where j,k are qubit indices and $k > j$. Additionally, Z^j is the Pauli-Z operator acting on qubit j,

$$Z = \begin{pmatrix} 1 & 0 \\ 0 & -1 \end{pmatrix}, \tag{A3}$$

and $\bar{g}_{jk}$ (g_{jk}) are the coupling coefficients of the resource (target) Hamiltonian. A method for other types of two-body Hamiltonians is given in [2], which, utilizing significantly more resources, is able to engineer target Hamiltonians with arbitrary Pauli operators using resource Hamiltonians with other arbitrary Pauli operators. In this manuscript we study algorithms that require only ZZ-type target Hamiltonians, so the assumptions of equations (A1) and (A2) are valid for our purposes.

An *analog block* is the multi-qubit entangling operation consisting on the evolution of all qubits under the resource Hamiltonian, for a finite and tunable time t,

$$U_{\bar{H}_{\mathcal{C}}}(t) = \exp\left(-i\, t \bar{H}_{\mathcal{C}}\right). \tag{A4}$$

The evolution unitary $U_{H_{\mathcal{C}}}$ under the target Hamiltonian $H_{\mathcal{C}}$, for some time t_f, is given by

$$U_{H_{\mathcal{C}}}(t_f) = \exp\left(-i\, t_f H_{\mathcal{C}}\right) \tag{A5}$$

$$= \exp\left(-i\, t_f \sum_{(j,k)\in\mathcal{C}} g_{jk} Z^j Z^k\right) \tag{A6}$$

$$= \prod_{(j,k)\in\mathcal{C}} \exp\left(-i\, t_f g_{jk} Z^j Z^k\right), \tag{A7}$$

which is equivalent to implementing c two-qubit $ZZ(\phi_{jk}$ gates as in equation (5) (see figure 6). The set of operations comprising such unitaries $U_{H_{\mathcal{C}}}$ and arbitrary SQGs is universal [1]. Therefore, any quantum algorithm can be written as a combination of SQGs and the evolution under such target Hamiltonians,

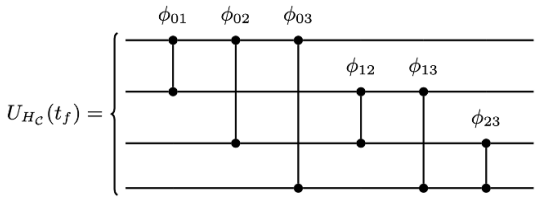

Figure 6. Digital circuit comprising $ZZ^{jk}(\phi_{jk})$ gates, equivalent to the evolution (A7) under a given target Hamiltonian (A2), for some time t_f, in a device with four qubits and ATA connectivity.

which themselves can be expressed as combinations of SQGs and analog blocks as we will explain in the following subsections. Thus, analog blocks along with SQGs are universal.

In the following subsections, we explain how one can effectively implement an arbitrary target Hamiltonian by making use of SQGs and a given resource Hamiltonian.

A.2. The stepwise digital–analog quantum circuit

The digital–analog quantum circuit we will describe in this subsection is constructed in the so-called *stepwise* DAQC (sDAQC) paradigm [1], as opposed to the *banged* DAQC (bDAQC) paradigm [1, 7] that will be discussed in appendix A.4. The defining characteristic of sDAQC is our ability to implement analog blocks with a defined beginning and end, by turning on and off all the interactions simultaneously.

The resource Hamiltonian's coupling coefficients $\{\bar{g}_{jk}\}_{(j,k)\in\mathcal{C}}$ are fixed by definition, though we assume that the qubits of the device can interact for a certain time t under the resource Hamiltonian in equation (A1) [1]. Because of this, we are only left with tuning the time of the evolution. The core idea of a DAQC protocol is to find a way to effectively engineer the desired coefficients of the target Hamiltonian, $\{g_{jk}\}$, by tuning the times of the analog blocks of a digital–analog quantum circuit (see equation (A4)), which can comprise analog blocks and SQGs. Inspired by the methods of [1, 3], we construct a digital–analog quantum circuit which contains c analog blocks, each running for some time t_{mn} (with the indices m, n running over the number of qubits, similarly to j, k), that implies a transformation

$$\{t_{mn}\}_{(m,n)\in\mathcal{C}} \longrightarrow \{g_{jk}\}_{(j,k)\in\mathcal{C}}\,. \tag{A8}$$

We will provide the method for calculating the appropriate runtimes $\{t_{mn}\}$ which effectively implement the correct coefficients $\{g_{jk}\}$ in appendix A.3, and for now concentrate on the construction of the DAQC circuit.

For the sake of clarity, we denote qubit indices as (j, k) or (m, n) as a shorthand notation for connected qubit pairs in the set $\mathcal{C}$. We start our considerations with a quantum circuit that consists of c analog blocks, each running for some time t_{mn}. In order to be able to implement a target Hamiltonian with arbitrary coefficients, firstly we need to effectively modify the signs of the coupling coefficients within each analog block. This is because we use the combined evolution of these different effective analog blocks, with modified signs, to engineer the arbitrary target Hamiltonian. To this end, we will interleave X gates in between the analog blocks, and make use of the identity [30]

$$X^a Z^b X^a = (-1)^{\delta_{ab}} Z^b\,, \tag{A9}$$

where X is the Pauli-X operator,

$$X = \begin{pmatrix} 0 & 1 \\ 1 & 0 \end{pmatrix}. \tag{A10}$$

Then, placing an X^a gate before and after an analog block has the effect of flipping the signs of all the terms in $\bar{H}_{\mathcal{C}}$ involving the qubit a, effectively implementing a different Hamiltonian, $\bar{H}'_{\mathcal{C}}$

$$U_{\bar{H}'_{\mathcal{C}}}(t) = X^a \exp\left(-it\bar{H}_{\mathcal{C}}\right) X^a \tag{A11}$$

$$= X^a \exp\left(-it\sum_{(j,k)} \bar{g}_{jk} Z^j Z^k\right) X^a \tag{A12}$$

$$= \exp\left(-it\sum_{(j,k)} \bar{g}_{jk} X^a Z^j Z^k X^a\right) \tag{A13}$$

$$= \exp\left(-it\sum_{(j,k)}(-1)^{\delta_{aj}+\delta_{ak}}\bar{g}_{jk}Z^jZ^k\right), \tag{A14}$$

where we have used the property $Re^{itH}R^\dagger = e^{itRHR^\dagger}$, provided that R is unitary [47]. Using this procedure, we can implement effective Hamiltonians that differ from the resource Hamiltonian by one or more sign flips, in each of the c analog blocks of the circuit.

Assume our quantum circuit is similar to that of figure 1, where each of the analog blocks is preceded and followed by X gates placed on the same connected qubits appearing in the connectivity $\mathcal{C}$. This specific way of placing the X gates will allow us in the next subsection to derive the explicit relationship between the times of the analog blocks and the coefficients of the target Hamiltonian. The evolution of a quantum state according to this circuit is given by

$$U_{\mathrm{DAQC}} = \prod_{(m,n)} X^mX^n\exp\left(-it_{mn}\bar{H}_{\mathcal{C}}\right)X^mX^n \tag{A15}$$

$$= \prod_{(m,n)} \exp\left(-it_{mn}X^mX^n\bar{H}_{\mathcal{C}}X^mX^n\right) \tag{A16}$$

$$= \prod_{(m,n)} \exp\left(-i\sum_{(j,k)} t_{mn}\bar{g}_{jk}X^mX^nZ^jZ^kX^mX^n\right). \tag{A17}$$

A.3. Runtimes of the analog blocks in stepwise DAQC

We now turn towards the calculation of the runtimes t_{mn} of the analog blocks. Utilizing equation (A9), we can write equation (A17) as

$$U_{\mathrm{DAQC}} = \prod_{(m,n)} \exp\left(-i\sum_{(j,k)} t_{mn}\bar{g}_{jk}(-1)^{\delta_{mj}+\delta_{mk}+\delta_{nj}+\delta_{nk}}Z^jZ^k\right) \tag{A18}$$

$$= \prod_{(m,n)} \exp\left(-i\sum_{(j,k)} t_{mn}\bar{g}_{jk}M_{mnjk}Z^jZ^k\right) \tag{A19}$$

$$= \exp\left(-i\sum_{(m,n)}\sum_{(j,k)} t_{mn}\bar{g}_{jk}M_{mnjk}Z^jZ^k\right). \tag{A20}$$

We have defined the tensor $M_{mnjk} \equiv (-1)^{\delta_{mj}+\delta_{mk}+\delta_{nj}+\delta_{nk}}$ containing c elements taking the values ± 1. We can convert these elements M_{mnjk} into a $c \times c$ matrix with entries $M_{\alpha\beta}$ by 'vectorizing' the pairs of coupled qubits $(m,n) \to \alpha; (j,k) \to \beta$ characterized by a single index each, as explained in appendix B. This also 'vectorizes' the times $t_{mn} \to \mathbf{t}$ and the coupling coefficients $\bar{g}_{jk} \to \bar{\mathbf{g}}$, $g_{jk} \to \mathbf{g}$.

The interpretation of the sign of a given element $M_{\alpha\beta}$ is the following: if $M_{\alpha\beta} = +1$ (-1), it means that the effective coupling corresponding to the αth coupling, during the βth analog block, is positive (negative).

Let us compare now equation (A20), which is the evolution we implement through the DAQC protocol, with equation (A7), which is the evolution under the target Hamiltonian we wish to simulate. They are equal if the following matrix equation is fulfilled,

$$\mathbf{G}\,t_f = M\mathbf{t}, \tag{A21}$$

where we define each element of $\mathbf{G}$ as $G_\beta \equiv \frac{g_\beta}{\bar{g}_\beta}$.

The runtimes of each analog block can therefore be calculated, such that, effectively, the time evolution under the target Hamiltonian is implemented, by inverting the matrix M,

$$\mathbf{t} = M^{-1}\mathbf{G}\,t_f. \tag{A22}$$

Equation (A22) allows us to find a vector of times $\mathbf{t}$ of the analog blocks such that the circuit described above effectively implements the evolution under the desired target Hamiltonian, provided that the matrix M is invertible. This invertibility must be studied on a case-by-case basis, and, in cases in which M is not invertible, the SQG placement may be shifted to produce a different matrix M, in this case invertible, while still making the DAQC protocol universal [1].

The case in which the resource Hamiltonian does not have only 2-body terms, but rather up to M-body terms with $M \geqslant 3$, is described in appendix C. Alternatively, an efficient way to effectively get rid of all odd-body terms (if present) in the resource Hamiltonian is explained in appendix D.

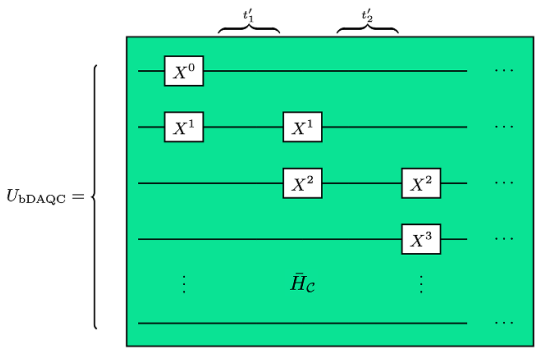

Figure 7. Schematic of the quantum circuit implementing a banged DAQC algorithm, with the analog evolution running throughout the whole computation. The analog block times t'_α in between SQGs have been modified according to equations (A23) and (A24).

A.4. Banged DAQC

In addition to sDAQC, which was described in the subsection above, another paradigm exists to perform an approximate DAQC, called *banged* DAQC (bDAQC) [1, 7]. The idea is that SQGs are applied simultaneously to an analog block, which runs throughout the whole circuit (see figure 7). The motivation behind bDAQC is that it does not require us to 'turn on and off' the analog Hamiltonian throughout the quantum circuit, but rather it stays constantly on from beginning to end. Repeatedly turning the analog blocks on and off introduces, for example, coherent errors such as leakage to non-computational states [12, 13]. In addition, such a procedure also suffers from calibration errors because each time an analog block is turned on, it needs a fine-tuned calibration of the control pulse parameters, upon which the unitary evolution is sensitive [11].

Consequently, a slight modification in the analog times between the layers of SQGs is required [1]. Specifically, for a quantum circuit with l analog blocks, the first and last (referred to as 'boundary') analog block times are modified by the single qubit gate duration Δt to

$$t'_{1,l} = t_{1,l} - \frac{3}{2}\Delta t, \tag{A23}$$

and the rest (referred to as 'central') of analog blocks' times are modified to

$$t'_\alpha = t_\alpha - \Delta t, \quad \alpha \in \{2, \ldots, l-1\}\,. \tag{A24}$$

The evolution under the simultaneous SQGs and analog block is given by

$$U_{\bar{H}+H_s}(\Delta t) = \exp\left(-i\Delta t[\bar{H} + H_s]\right), \tag{A25}$$

where H_s is the Hamiltonian that generates the SQGs. In general, $\bar{H}$ and H_s might not commute. This introduces a reverse Trotter error [1], due to which the bDAQC computation is not exactly equal to the evolution generated by the target Hamiltonian anymore. This error depends, among other things, on the duration of the SQGs Δt, and it is different for the boundary analog blocks and for the central analog blocks, due to different Trotterization methods. Keep in mind that, usually, the term Trotter error is used in the case in which the ideal evolution is that of non-commuting Hamiltonians acting simultaneously, and is introduced when 'splitting' it into sequential evolutions under each individual Hamiltonian [48, 49]. However, we use it in the reverse case: the ideal evolution is that of the sequential application of the Hamiltonians, and the error is introduced when applying them simultaneously.

Consequently, there is a trade-off between the errors arising from turning on and off the analog blocks being eliminated, and the Trotter error being introduced.

We study this intrinsic error associated with bDAQC, and its scaling, in more detail in section 3.4.

Appendix B. The sign matrix M

The set of elements M_{mnjk} has four indices. Let us 'reorder' these elements in such a way that they can be arranged into a matrix, so that we will be able to invert it. In order to do that, we *vectorize* the pairs of indices $(m,n) \to \alpha$ and $(j,k) \to \beta$, assigning to each pair a single number, ordered from smallest to biggest m (j), then from smallest to biggest n (k). For example, for an ATA 3-qubit device:

$$(m,n) = (0,1) \to \alpha = 1\,, \tag{B1}$$

$$(m,n) = (0,2) \rightarrow \alpha = 2\,, \tag{B2}$$

$$(m,n) = (1,2) \rightarrow \alpha = 3\,. \tag{B3}$$

This way, each pair of indices (m,n) is uniquely mapped to a single index α. The same is done with each pair of indices (j,k), which is uniquely mapped into a single index β. This way, we are also able to map M_{mnjk} to $M_{\alpha\beta}$.

The general formula for this mapping in the ATA case for N qubits is [1]

$$(m,n) \rightarrow \alpha = N(m-1) - m(m+1)/2 + n\,, \tag{B4}$$

$$(j,k) \rightarrow \beta = N(j-1) - j(j+1)/2 + k\,. \tag{B5}$$

On the other hand, the inverse transformation $\alpha \rightarrow (m,n)$ is given by:

$$n = 1 + H_1\left[\frac{\alpha}{N}\right] + H_1\left[\frac{\alpha}{2N-2}\right] + H_1\left[\frac{\alpha}{3N-5}\right] + \cdots + H_1\left[\frac{\alpha}{N(N-1)/2}\right], \tag{B6}$$

$$m = \alpha - N(n-1) + \frac{n(n+1)}{2}, \tag{B7}$$

where H_1 is the Heaviside step function at 1,

$$H_1[x] = \begin{cases} 0 & x < 1 \\ 1 & x \geqslant 1 \end{cases} \tag{B8}$$

Note that these inverse transformations are incorrect in [1].

Appendix C. DAQC for Hamiltonians with up to M-body terms

In appendix A, we have laid out a method for performing DAQC using an Ising Hamiltonian with two-body terms. In this section, we generalize this method for the case of resource Hamiltonians that have additional, up to M-body terms. We characterize such a Hamiltonian by the collection of pairs of connected qubits $(j,k) \in \mathcal{C}_2$, the collection of triplets of connected qubits $(j,k,l) \in \mathcal{C}_3$... in general, $\mathcal{C}_b$, and their corresponding coupling strengths $\bar{g}^b$

$$\bar{H}_M = \sum_{(j,k)} \bar{g}^2_{jk} Z^j Z^k + \sum_{(j,k,l)} \bar{g}^3_{jkl} Z^j Z^k Z^l + \cdots \tag{C1}$$

Each $\mathcal{C}_b$ has c_b elements. This way, the total connectivity of the M-body resource Hamiltonian is

$$\mathcal{C} = \bigcup_{b=2}^{M} \mathcal{C}_b\,, \tag{C2}$$

which has a total of $c = \sum_b^M c_b$ elements. As a specific example, the total number of terms, c, appearing in an ATA Hamiltonian with up to M-body terms is given by:

$$c = \binom{N}{2} + \binom{N}{3} + \ldots + \binom{N}{M}. \tag{C3}$$

If we are able to use the resource Hamiltonian (C1) to implement an arbitrary target Hamiltonian with the same structure,

$$H_M = \sum_{(j,k)} g^2_{jk} Z^j Z^k + \sum_{(j,k,l)} g^3_{jkl} Z^j Z^k Z^l + \ldots\,, \tag{C4}$$

then we can get rid of the higher body terms by setting $g^b = 0$ for all $b > 2$. Alternatively, if our problem at hand has such higher body terms, we can use them to our advantage. Such interaction terms may appear, e.g in fermionic [50, 51] and lattice gauge theory quantum simulations [52], and quantum optimization [53–55].

Let us construct a digital–analog quantum circuit consisting of c analog blocks. The first c_2 analog blocks are preceded and followed by $X^m X^n$ gates, in exactly the same way as described in appendix A (see figure 1).

The following c_3 analog blocks are preceded and followed by $X^m X^n X^p$ gates, with $(m,n,p) \in \mathcal{C}_3$. This pattern is repeated until the analog blocks are exhausted. This quantum circuit is a generalization of the one described in appendix A, for which we were restricting ourselves to $\mathcal{C} = \mathcal{C}_2$.

This way, the unitary evolution of such a circuit is

$$\begin{aligned} U_{DAQC} = &\prod_{(m,n)} X^m X^n \exp\left(i\, t^2_{mn} \left[\sum_{(j,k)} \bar{g}^2_{jk} Z^j Z^k + \sum_{(j,k,l)} \bar{g}^3_{jkl} Z^j Z^k Z^l + \dots \right] \right) X^m X^n \\ &\times \prod_{(m,n,p)} X^m X^n X^p \exp\left(i\, t^3_{mnp} \left[\sum_{(j,k)} \bar{g}^2_{jk} Z^j Z^k + \sum_{(j,k,l)} \bar{g}^3_{jkl} Z^j Z^k Z^l + \dots \right] \right) X^m X^n X^p \cdots \end{aligned} \tag{C5}$$

$$\begin{aligned} = &\prod_{(m,n)} \exp\left(i\, t^2_{mn} \left[\sum_{(j,k)} M^{(2,2)}_{jkmn} \bar{g}^2_{jk} Z^j Z^k + \sum_{(j,k,l)} M^{(3,2)}_{jklmn} \bar{g}^3_{jkl} Z^j Z^k Z^l + \dots \right] \right) \\ &\times \prod_{(m,n,p)} \exp\left(i\, t^3_{mnp} \left[\sum_{(j,k)} M^{(2,3)}_{jkmnp} \bar{g}^2_{jk} Z^j Z^k + \sum_{(j,k,l)} M^{(3,3)}_{jklmnp} \bar{g}^3_{jkl} Z^j Z^k Z^l + \dots \right] \right) \cdots , \end{aligned} \tag{C6}$$

where we have introduced the collections of elements $M^{(a,b)}_{jk\dots mn\dots}$, which can take on the values ± 1. These elements are calculated as

$$M^{(a,b)}_{jk\dots mn\dots} = (-1)^{\alpha}, \text{where } \alpha = \sum_{\substack{\nu=\{j,k\dots\} \\ \mu=\{m,n\dots\}}} \delta_{\nu\mu}, \tag{C7}$$

for which the ones in equation (A20) are a special case with $\nu = \{i,j\}$ and $\mu = \{m,n\}$. Now, each of these collections of elements can be rearranged into a matrix $M^{(a,b)}$ of dimensions $c_a \times c_b$, following a process similar to the one in appendix B. When comparing our DAQC evolution (C6) and the evolution under the target Hamiltonian (C4) for some time t_f, we can see that they are equal when the following set of matrix equations holds:

$$\begin{aligned} t_f \mathbf{G}^2 &= M^{(2,2)}\, \mathbf{t}^2 + M^{(2,3)}\, \mathbf{t}^3 + \cdots \\ t_f \mathbf{G}^3 &= M^{(3,2)}\, \mathbf{t}^2 + M^{(3,3)}\, \mathbf{t}^3 + \cdots \\ \vdots \quad &= \quad \vdots \quad + \quad \vdots \quad + \ddots \end{aligned} \tag{C8}$$

Again, equation (A21) is a special case of this set of equations, in which we restrict ourselves only to the first term of the RHS of the first equation. This set of equations can be written as just one matrix equation, where a *joint* matrix of dimensions $c \times c$ appears, comprising all the $M^{(a,b)}$ matrices:

$$t_f \begin{pmatrix} \mathbf{G}^2 \\ \mathbf{G}^3 \\ \vdots \end{pmatrix} = \begin{pmatrix} M^{(2,2)} & M^{(2,3)} & \cdots \\ M^{(3,2)} & M^{(3,3)} & \cdots \\ \vdots & \vdots & \ddots \end{pmatrix} \begin{pmatrix} \mathbf{t}^2 \\ \mathbf{t}^3 \\ \vdots \end{pmatrix}, \tag{C9}$$

which we can write as $t_f \mathbf{G}_{\text{joint}} = M_{\text{joint}} \mathbf{t}_{\text{joint}}$ for compactness. By solving this equation through the inversion of the *joint* matrix M_{joint}, we can calculate the time each analog block must run for in our digital–analog circuit:

$$\mathbf{t}_{\text{joint}} = M^{-1}_{\text{joint}} \mathbf{G}_{\text{joint}} t_f. \tag{C10}$$

Expressing the relationship between the times and the couplings of the target Hamiltonian in this single equation is very useful, because then the only condition we need to impose for this relation to hold is the invertibility of the *joint* matrix, as opposed to the invertibility of each individual $M^{(a,b)}$ matrix.

Appendix D. Cancelling undesired odd-body terms in the resource Hamiltonian

By substituting an analog block of time t by two analog blocks of time $t/2$ each, and placing X gates on all qubits before and after one of the two analog blocks (see figure 8), we can effectively cancel all odd-body

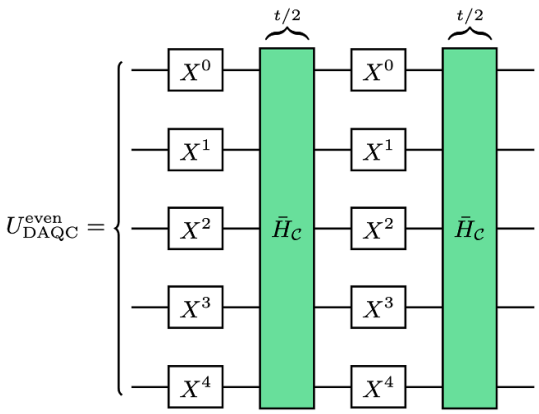

Figure 8. Digital–analog circuit implementing an analog block with all odd-body terms cancelled, for a five-qubit device.

terms. This is because flipping the sign of the couplings of all qubits leaves the even-body terms untouched, but flips the sign of all odd-body terms, as exemplified here for two- and three-body terms:

$$\left(\prod_{m=0}^{N} X^m\right) Z^j Z^k \left(\prod_{m=0}^{N} X^m\right) = (-1)^2 Z^j Z^k = Z^j Z^k, \tag{D1}$$

$$\left(\prod_{m=0}^{N} X^m\right) Z^j Z^k Z^l \left(\prod_{m=0}^{N} X^m\right) = (-1)^3 Z^j Z^k Z^l = -Z^j Z^k Z^l. \tag{D2}$$

Thus, evolving by times $t/2$ with the original and flipped signs cancels all odd-body terms, while evolving according to all even-body terms for a total time t. This procedure introduces, at most, $2N$ single-qubit gates (SQGs) per analog block, while leaving the total analog times intact. The SQG depth is increased, at most, by two per analog block.

Appendix E. Resource Hamiltonian with superconducting qubits

One of the leading platforms for large-scale quantum computing are superconducting circuits based on transmon qubits [20, 56, 57]. More recently, *tunable coupler* [58] based architectures have become the leading transmon platform [20, 56, 59, 60] due to their ability to better control the qubit interactions [12]. Moreover, such architectures natively implement an adiabatic ZZ interaction [61], as required for the implementation of DAQC with the resource Hamiltonian from equation (1). However, [62] has demonstrated that when taking into account the fabrication precision, transmon arrays (without tunable couplers) may exhibit significant many-body interactions in the idling regime, suggesting that implementing sufficiently strong, purely two-body interactions is not straightforward. We therefore analyze whether current state-of-the-art transmon processors with tunable couplers can mitigate this issue and be used to implement the two-body resource Hamiltonian from equation (1).

To this purpose, we model each transmon as an anharmonic oscillator of the form $H_i = \omega_i a_i^\dagger a_i + \frac{\alpha_i}{2} a_i^\dagger a_i^\dagger a_i a_i$, where $a_i^{(\dagger)}$ are bosonic annihilation (creation) operators of the transmon with index i, ω_i is its frequency, and α_i is its anharmonicity. The interactions between the transmons are implemented via capacitive coupling, modeled via the interaction Hamiltonian $H_{ij} = -g_{ij}(a_i^\dagger - a_i)(a_j^\dagger - a_j)$, where the coupling constant $g_{ij} = \beta_{ij}\sqrt{\omega_i \omega_j}$, where β_{ij} is a constant dependent on the capacitances of the transmons. The tunable coupler is implemented via an additional transmon, with the main difference being that the frequency of the tunable coupler ω^{c} can be tuned via the application of external magnetic flux, thus inducing or cancelling any interaction between computational transmons. In order to distinguish the tunable coupler transmons from the computational transmons, we will use the annihilation (creation) operators $b_i^{(\dagger)}$ for the tunable coupler degrees of freedom. All together the Hamiltonian of a system of N_{q} computational transmons (indexed with q) coupled via N_{c} tunable couplers (indexed with c) is the sum of terms representing each computational transmon (H_i^{q}), tunable coupler (H_i^{c}) and the capacitive coupling terms

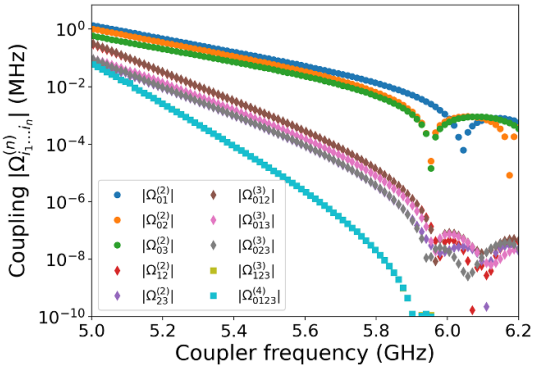

Figure 9. Absolute values of all possible couplings $\Omega^{(n)}_{i_1\ldots i_n}$ defined in equation (E3), on a four-qubit star architecture (see figure 10 for the qubit labeling). For simplicity, the frequencies of all coupler transmons (on the x-axis) are equal. Different marker shapes are used to discern between couplings of different orders. The parameters of the Hamiltonian in equation (E2) are inspired by the experimental implementations in [12, 63]. More specifically, $\omega^{\mathrm{q}}_{0,1,2,3} = [4.571, 4.734, 4.728, 4.725]$ GHz, $\alpha^{\mathrm{q}}_{0,1,2,3} = [-0.200, -0.199, -0.196, -0.208]$ GHz, $\alpha^{\mathrm{c}}_{(0,1),(0,2),(0,3)} = [-0.094, -0.098, -0.099]$ GHz with the dimensionless coupling coefficients $\beta^{\mathrm{qc}}_{(0,1),(0,2),(0,3)} = [0.0149, 0.0146, 0.0150]$, $\beta^{\mathrm{cq}}_{(0,1),(0,2),(0,3)} = [0.0154, 0.0151, 0.0150]$, $\beta^{\mathrm{qq}}_{(0,1),(0,2),(0,3)} = [0.001, 0.001, 0.001]$.

between all the elements (H^{qc}_{ij}, H^{cq}_{ij} and H^{qq}_{ij}), or more explicitly

$$H_{\mathrm{full}} = H_{\mathrm{q}} + H_{\mathrm{c}} + H_{\mathrm{qc}} + H_{\mathrm{cq}} + H_{\mathrm{qq}} \tag{E1}$$

$$\begin{aligned} &= \hbar \sum_{i=1}^{N_{\mathrm{q}}} \left(\omega^{\mathrm{q}}_i a^\dagger_i a_i + \frac{\alpha^{\mathrm{q}}_i}{2} a^\dagger_i a^\dagger_i a_i a_i \right) \\ &+ \hbar \sum_{i=1}^{N_{\mathrm{c}}} \left(\omega^{\mathrm{c}}_i b^\dagger_i b_i + \frac{\alpha^{\mathrm{c}}_i}{2} b^\dagger_i b^\dagger_i b_i b_i \right) \\ &+ \hbar \sum_{(i,j)} g^{\mathrm{qc}}_{ij} \left(a^\dagger_i - a_i \right) \left(b^\dagger_j - b_j \right) \\ &+ \hbar \sum_{(i,j)} g^{\mathrm{cq}}_{ij} \left(b^\dagger_i - b_i \right) \left(a^\dagger_j - a_j \right) \\ &+ \hbar \sum_{(i,j)} g^{\mathrm{qq}}_{ij} \left(a^\dagger_i - a_i \right) \left(a^\dagger_j - a_j \right), \end{aligned} \tag{E2}$$

with the sum over coupled transmons denoted by $\sum_{(i,j)}$. Crucially, the qubit degrees of freedom are encoded in the eigenstates of the Hamiltonian in equation (E2), and identified via the maximum overlap rule [12]. After removing the single-qubit terms, the interaction part of the qubitized Hamiltonian is

$$H_{\mathrm{qb}} = \sum_{i,j=1}^{N_{\mathrm{q}}} \Omega^{(2)}_{ij} Z_i Z_j + \sum_{i,j,k=1}^{N_{\mathrm{q}}} \Omega^{(3)}_{ijk} Z_i Z_j Z_k + \sum_{i,j,k,l=1}^{N_{\mathrm{q}}} \Omega^{(4)}_{ijkl} Z_i Z_j Z_k Z_l + \ldots, \tag{E3}$$

also known as the τ-Hamiltonian in the context of many-body localization theory [62]. The vector of the eigenenergies $\mathbf{E}$ of the Hamiltonian from equation (E2) restricted to the computational basis is related to the coefficients $\Omega^{(n)}_{i_1\ldots i_n}$ via the dot product $\Omega^{(n)}_{i_1\ldots i_n} = 2^{-N_{\mathrm{q}}} \mathbf{E} \cdot \mathbf{Z}_{i_1\ldots i_n}$, where $\mathbf{Z}_{i_1\ldots i_n}$ is the diagonal of the corresponding N_{q}-qubit Pauli operator [62]. We perform this analysis for $N_{\mathrm{q}} = 4$ computational transmons arranged in a star connectivity and plot the magnitudes of the coupling coefficients $\Omega^{(n)}_{i_1\ldots i_n}$ in figure 9.

Figure 9 displays the effective Z-type couplings as the interaction is turned 'on' by tuning the coupler frequencies $\omega^{\mathrm{c}}_{(0,1),(0,2),(0,3)}$ closer to the qubit frequencies $\omega^{\mathrm{q}}_{0,1,2,3}$. The results in figure 9 clearly indicate a hierarchy of coupling strengths, as also observed in [62]. The most prominent are the desired two-qubit couplings between the directly coupled qubits and the strongest parasitic couplings are the two-qubit couplings between uncoupled transmons and 3-body interactions between directly coupled qubits. We can clearly see that the magnitude of the parasitic couplings represents a significant fraction of the desired interaction strength, especially at larger desired coupling strengths. Figure 9 therefore reveals an inherent trade-off where stronger desired interactions will induce larger errors due to parasitic coupling terms, but weaker two-body interactions will also require longer analog block durations, making the system more

vulnerable to decoherence. The presented results demonstrate that, even with the introduction of tunable couplers, the implementation of a purely two-body Hamiltonian in an array of capacitively coupled transmons remains challenging.

Appendix F. Derivation of bDAQC non-commutativity error

In reference [1], it is shown that the first and last analog blocks (i.e. a constant number of analog blocks) of a digital–analog circuit introduce errors $e_{\text{boundary}} = \mathcal{O}(\Delta t^2)$.

Each central analog block, however, is shown to introduce an error

$$e_{\text{central}} = \left\| 1 - e^{-i\bar{H}\Delta t/2} e^{-iH_s\Delta t} e^{-i\bar{H}\Delta t/2} e^{i(\bar{H}+H_s)\Delta t} \right\| \tag{F1}$$

$$= \frac{(\Delta t)^3}{4} \left\| [[\bar{H}, H_s], \bar{H} + 2H_s] \right\| + \mathcal{O}\left(\Delta t^4\right), \tag{F2}$$

where H_s is the Hamiltonian generating the SQG that overlaps the resource Hamiltonian. Let's assume that this SQG is an X^a gate, and thus $H_s = \frac{\pi}{2\Delta t} X^a$. By explicitly plugging this, and the resource Hamiltonian $\bar{H} = \sum_{j,k} \bar{g}_{jk} Z^j Z^k$ into (F2), we can get the explicit expression of e_{central}. The innermost commutator in equation (F2) is

$$[\bar{H}, H_s] = \left[\sum_{k=1}^{d} \bar{g} Z^a Z^k, \frac{\pi}{2\Delta t} X^a \right] \tag{F3}$$

$$= \frac{\mathrm{d}\bar{g}\pi}{2\Delta t} \left[Z^a Z^k, X^a \right] \tag{F4}$$

$$= \frac{\mathrm{d}\bar{g} i\pi}{\Delta t} Y^a Z^k. \tag{F5}$$

Plugging this into the outermost commutator yields

$$[[\bar{H}, H_s], \bar{H} + 2H_s] = \frac{\mathrm{d}\bar{g}\pi i}{\Delta t} \left[Y^a Z^k, \bar{H} + 2H_s \right] \tag{F6}$$

$$= \frac{\mathrm{d}\bar{g}\pi i}{\Delta t} \left(\left[Y^a Z^k, \bar{H} \right] + \left[Y^a Z^k, 2H_s \right] \right). \tag{F7}$$

Each of the two commutators above yields:

$$[Y^a Z^a, \bar{H}] = \left[Y^a Z^a, \sum_{k=1}^{d} \bar{g} Z^a Z^k \right] \tag{F8}$$

$$= 2d\bar{g} i X^a I^k \tag{F9}$$

$$[Y^a Z^a, 2H_s] = \left[Y^a Z^a, \frac{\pi}{\Delta t} X^a \right] \tag{F10}$$

$$= \frac{-2\pi i}{\Delta t} Z^a Z^k. \tag{F11}$$

Computing the total infidelity, we get

$$e_{\text{central}} = \frac{(\Delta t)^3}{4} \sqrt{(d\bar{g})^4 \left(\frac{2\pi}{\Delta t} \right)^2 + (2d\bar{g})^2 \left(\frac{\pi}{\Delta t} \right)^4}. \tag{F12}$$

Appendix G. Detailed error analysis of digital–analog QFT and GHZ state preparation

G.1. ATA-QFT error analysis

In order to translate the digital QFT into the digital–analog paradigm, we must first identify the target Hamiltonians we need to implement. We do that by taking the biggest blocks of consecutive $ZZ(\phi)$ gates. As an example, we show the first and last such target Hamiltonians for the ATA-QFT in figure 3(a), and from that it becomes clear that $N-1$ such blocks are needed.

The sources of possible errors were specified in section 3 and their effects on the compound fidelity summarized in equations (16) and (18). For an ATA device, the number of couplings c is given by $c = N(N-1)/2$. For the digital–analog ATA-QFT, we therefore find the following scaling behavior with the number of qubits N:

1. **Number of analog blocks:** the ATA-QFT circuit is constructed as $\mathcal{O}(N)$ target Hamiltonians. Each target Hamiltonian requires $c = \mathcal{O}(N^2)$ analog blocks (see section 3.1). Thus, the total number of analog blocks is $\mathcal{O}(N^3)$.
2. **Number of two-qubit terms:** each analog block contains $c = \mathcal{O}(N^2)$ two-qubit terms (see section 3.1.2). Thus, the total number of two qubit terms in all the analog blocks is $\mathcal{O}(N^5)$.
3. **Duration:** the digital ATA-QFT can be implemented in depth $\mathcal{O}(N)$ [64, 65]. On the other hand, the total duration of the DAQC algorithm depends on the resulting matrix M for each case, and thus we cannot say anything about it *a priori* (see section 3.2). We numerically compute the duration of this algorithm in section 5, and, by fitting a curve to the simulated data, we extract a scaling of the duration $\mathcal{O}(N^{2.05})$.
4. **Number of SQGs:** each target Hamiltonian requires $c = \mathcal{O}(N^2)$ X gates (see section 3.3). Thus, the total number of SQGs is $\mathcal{O}(N^3)$.
5. **bDAQC non-commutativity:** each qubit has a degree $d = \mathcal{O}(N)$, so from equation (12), and setting $\Delta t, \bar{g}$ to be constant, each analog block introduces an error that scales as $\epsilon_{\text{central}} = \mathcal{O}(N^2)$ (see section 3.4). There are $\mathcal{O}(N^3)$ analog blocks, so the contribution from bDAQC to the compound fidelity in equation (18) scales as $(1 - \mathcal{O}(N^2))^{\mathcal{O}(N^3)}$.

The worse error scaling for DAQC in the case of ATA-QFT is, in part, a result of the sparsity of two-qubit terms in QFT. DQC requires only one TQG for each non-zero term of the target Hamiltonians; however, DAQC is introducing *superfluous* analog blocks needed to effectively cancel the non-zero couplings of the resource Hamiltonian. On top of that, each of these analog blocks introduces a large number of two-qubit terms, as compared to just one two-qubit term per TQG.

G.2. Star-QFT error analysis

In this subsection, we analyze the scaling of the error sources for the digital–analog QFT implemented on a star-connectivity, using the optimized protocol of appendix H, and work out the improvement compared to the ATA-QFT.

Implementing the QFT on a star-connectivity introduces the need for SWAP gates placed between each target Hamiltonian, as can be seen in figure 3(b), and each SWAP gate requires six additional analog blocks when translated to a digital–analog implementation (see appendix I).

For a star-connectivity device, the number of couplings c is again given by $c = N - 1$. For the digital–analog star-QFT, we therefore find the following scaling behavior with the number of qubits N:

1. **Number of analog blocks:** similarly to the ATA-QFT, the star-QFT circuit is constructed as $\mathcal{O}(N)$ target Hamiltonians. However, in this case, each target Hamiltonian requires $c = \mathcal{O}(N)$ analog blocks, because the other analog blocks get cancelled. On the other hand, in total, the need for $\mathcal{O}(N)$ SWAP gates introduces $\mathcal{O}(N)$ analog blocks. Thus, the total number of analog blocks is $\mathcal{O}(N^2)$.
2. **Number of two-qubit terms:** each analog block contains $c = \mathcal{O}(N)$ two-qubit terms. Therefore, the total number of two-qubit terms in all the analog blocks is $\mathcal{O}(N^3)$.
3. **Duration:** the digital star-QFT can be implemented in depth $\mathcal{O}(N^2)$. In the digital–analog circuit, the nth target Hamiltonian has n null coupling coefficients (meaning that $g_{jk} = 0$), which eliminates $n - 1$ analog blocks (recalling the discussion of equation (H4)). In addition, the difference between one coupling coefficient and the next decreases exponentially (see the exponentially decreasing phases in figure 3(b)). Recall from equation (H4) that the analog times are proportional to the difference between the coefficient of each term in the Hamiltonian and the following. Thus, the contribution to the analog times of each target Hamiltonian is asymptotically constant, and the duration of the whole algorithm is decreased to $\mathcal{O}(N)$.
4. **Number of SQGs:** each target Hamiltonian requires $\mathcal{O}(N)$ X gates. Thus, the total number of SQGs is $\mathcal{O}(N^2)$.
5. **bDAQC non-commutativity:** each external qubit, on which X gates are applied, has one coupling, so from equation (12), each analog block introduces an infidelity that scales as $\mathcal{O}(1)$, when $\Delta t, \bar{g}$ are set to be constant. There are $\mathcal{O}(N^2)$ analog blocks, so the contribution to the compound fidelity (see equation (18)) introduced by bDAQC scales as $(1 - \mathcal{O}(1))^{\mathcal{O}(N^2)}$.

The errors for star-QFT scale slower when compared to the ATA-QFT, but the scaling is generally still worse than in DQC. This is because, even though the number of analog blocks scales similarly to the number

of TQGs required for the DQC algorithm, each analog block introduces more two-qubit terms that are prone to mischaracterization.

In this case, the duration of the algorithm scales linearly in DAQC while it scales quadratically in DQC, so it presents an advantage in that regard. Additionally, the intrinsic error introduced by bDAQC is smaller than that introduced by the two-qubit terms, so bDAQC has the potential of a bigger improvement than in the ATA case.

Appendix H. Optimized DAQC on a device with a star-connectivity

As discussed in the previous section, some of the error sources present in DAQC are sensitive to the number of analog blocks required within the protocol, and to the total time of the quantum circuit.

While the protocol described in [1] can work for any arbitrary connectivity, ad hoc protocols can be developed for specific connectivities using fewer analog blocks and, consequently, shorter algorithm runtimes. For example, in [3], an optimized DAQC protocol is developed for a device with a nearest-neighbors connectivity in an open, one-dimensional graph, which reduces the number of analog blocks, and also their runtimes.

On the other hand, we focus on a device with a so-called star-connectivity, where a *central* qubit is coupled to $N-1$ other *external* qubits (see figure 10(a)). We can write said connectivity as $\mathcal{S} = \{(0,1),(0,2),\ldots,(0,N-1)\}$, where we label the central qubit with index 0. Algaba *et al* [66], e.g describes how an effective star-connectivity device can be built out of superconducting circuits.

The main idea behind the optimized DAQC protocol [3] is to place the X gates in such a way that we obtain an $(N-1)\times(N-1)$ sign matrix M, that relates the coupling coefficients of the resource and target Hamiltonians to the analog times according to equation (4), of the form

$$M = \begin{pmatrix} 1 & 1 & 1 & \cdots & 1 & 1 & 1 \\ -1 & 1 & 1 & \cdots & 1 & 1 & 1 \\ -1 & -1 & 1 & \cdots & 1 & 1 & 1 \\ \vdots & \vdots & \vdots & \ddots & \vdots & \vdots & \vdots \\ -1 & -1 & -1 & \cdots & 1 & 1 & 1 \\ -1 & -1 & -1 & \cdots & -1 & 1 & 1 \\ -1 & -1 & -1 & \cdots & -1 & -1 & 1 \end{pmatrix}, \tag{H1}$$

i.e. a matrix with its elements being 1 on and above the diagonal, and -1 below the diagonal.

Recall the definition of the vector $\mathbf{G}$ from equation (4), with elements $G_\beta = g_\beta/\bar{g}_\beta$. We reorder and express, without loss of generality, the elements of vector $\mathbf{G}$ in such a way that the following conditions are met,

$$G_\beta \geqslant 0\,, \tag{H2}$$

$$G_\beta \geqslant G_{\beta+1}\,. \tag{H3}$$

For the first condition to be met, we may need to shift the phase of the evolution, $\phi_\beta \to \phi'_\beta = \phi_\beta - 2\pi$, in order to change the signs of the target coefficients (recall that $\phi_\beta = t_f g_\beta \mod (2\pi)$). Through this transformation, we can change the sign of G_β without affecting said unitary evolution. For the second condition, we may need to change the order of the labels of the coefficients in $\mathbf{G}$. Under these conditions, it is proven in [3] that the inverse M^{-1} yields runtimes for the analog blocks (see equation (4)) given by

$$\frac{t_\alpha}{t_f} = \frac{G_\alpha - G_{\alpha+1}}{2}\,, \tag{H4}$$

$$\frac{t_{N-1}}{t_f} = \frac{G_1 + G_{N-1}}{2}\,. \tag{H5}$$

Also in [3], it is proven that these equations lead to the minimum number of analog blocks, running for a minimal time, required to implement a given target Hamiltonian. One can see in equation (H4) how the number of analog blocks gets reduced if k elements of $\mathbf{G}$ are equal, which makes $k-1$ elements of $\mathbf{t}$ equal to zero. Also, one can see how the time of each analog block t_α gets reduced as the difference between G_α and $G_{\alpha+1}$ gets smaller. Then, our task is to find the correct placement of the X gates in our digital–analog circuit, in order to obtain an M matrix of the form (H1) for a star-connectivity.

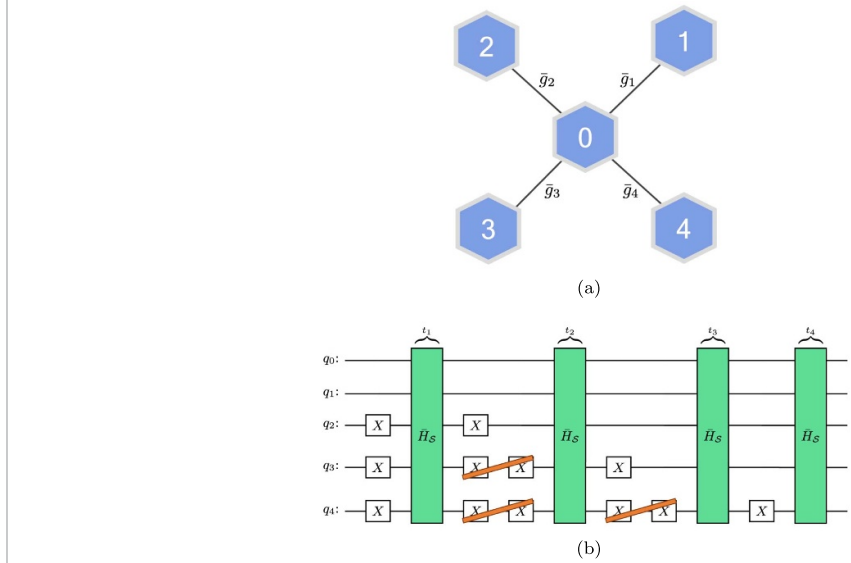

Figure 10. (a) Scheme of a five qubit device with star-connectivity. Each node corresponds to a qubit, and each edge to a coupling (i.e. to a $\bar{g}_j Z^0 Z^j$ term in $\bar{H}_S$). (b) Quantum circuit for an optimized sDAQC protocol on a star-connectivity device with five qubits.

According to the interpretation of the M matrix from appendix A.3, a digital–analog quantum circuit corresponding to the matrix M can be constructed by flipping all but one couplings in the first analog block, and flipping one less coupling in the subsequent analog blocks. An example of such a circuit for 5 qubits is given in figure 10.

Additionally, recall our discussion of non-commutativity errors in bDAQC in section 3.4 and their dependence on the qubits' degree. This protocol also minimizes the number of overlapping $Z^j Z^a$ terms with the X^a gates introduced, given that they are only acting on the *external* qubits, which have degree $d = 1$. Compared against other connectivities, qubits in an ATA connectivity have $d = N - 1$, and in a one-dimensional chain they have $d = 2$. Thus, this protocol also minimizes the error introduced by the non-commutativity of the resource Hamiltonian and the single-qubit terms.

Such optimized protocols have been described only for the one-dimensional open chain (in [3]) and for the star-connectivity (in this manuscript) so far. This is because, in general, it is not possible to change the sign of just one coupling in an arbitrary connectivity without changing the others, which is required to get the necessary M matrix (H1). Take, for example, a square lattice: to flip a coupling between two qubits, we place X gates on one of the qubits involved, but this flips three additional couplings. To correct these additional flipped signs, we can place X gates on the three other qubits involved, but this flips three additional signs each. For such a reason, it is not possible to flip the sign of a coupling in an isolated way in an arbitrary connectivity.

Appendix I. Digital–analog SWAP gates on a star-connectivity

The SWAP gate acts on two qubits by exchanging their states, $|j\rangle|k\rangle \to |k\rangle|j\rangle$

$$\mathrm{SWAP} = \begin{pmatrix} 1 & 0 & 0 & 0 \\ 0 & 0 & 1 & 0 \\ 0 & 1 & 0 & 0 \\ 0 & 0 & 0 & 1 \end{pmatrix}. \tag{I1}$$

A SWAP gate applied on the central qubit and one of the external qubits can be expressed in terms of two-qubit Pauli rotations as:

$$\mathrm{SWAP} = \exp\left(i\frac{\pi}{4}\left(X^0X^k + Y^0Y^k + Z^0Z^k\right)\right) \tag{I2}$$

$$= \exp\left(i\frac{\pi}{4}X^0X^k\right)\exp\left(i\frac{\pi}{4}Y^0Y^k\right)\exp\left(i\frac{\pi}{4}Z^0Z^k\right) \tag{I3}$$

$$= \left[H^0H^k\exp\left(i\frac{\pi}{4}Z^0Z^k\right)H^0H^k\right] \times \left[S^0S^kH^0H^k\exp\left(i\frac{\pi}{4}Z^0Z^k\right)H^kH^0S^{\dagger k}S^{\dagger 0}\right] \times \exp\left(i\frac{\pi}{4}Z^0Z^k\right). \tag{I4}$$

In the last equality, we have decomposed the SWAP gate into three different evolutions under a Z^0Z^k Hamiltonian, each of which we can interpret as a target Hamiltonian with all couplings $g_{jk} = 0$ except for $g_{0k} = \frac{\pi}{4t_f}$. Following the optimized DAQC protocol described in appendix H, each of these target Hamiltonians requires two analog blocks, accounting for a total of 6 analog blocks needed to implement a SWAP gate.

Appendix J. Trade-off between control errors and environmental noise in star-QFT

While the DQC algorithm for the star-QFT has a better performance than DAQC regarding the infidelity coming from control errors (see figure 5(b)), it has a longer execution time (see figure 5(e)). In turn, long execution times imply that the algorithm becomes more affected by environmental decoherence, so a trade-off may arise for a large enough number of qubits, in which decoherence accounts for a bigger effect on the infidelity.

Table 2. Parameters of the fitting of the curve (J2) to the data in figure 11. The parameter f is smaller for DAQC in part because, even though the fidelity per two-qubit term was chosen to be higher for DAQC in the simulations, their successive action on the same pairs of qubits throughout the algorithm accumulates coherent errors, thus effectively decreasing their overall fidelity [36]. Similarly, the parameter b is worse than the scaling of the number of two-qubit terms predicted in appendix G.2 for the three paradigms because of this accumulation of coherent errors, and from the absorption of the secondary sources of error into a single parameter.

	f	a	b	c
DQC	0.99986	0.92985	2.3882	-1.58×10^{-4}
sDAQC	0.99831	0.06445	3.8571	-2.94×10^{-4}
bDAQC	0.99858	0.42443	2.8559	-0.02373

In order to analyze such a trade-off, we study the relationship between the scaling of both sources of infidelity. We assume, like we did in section 3.5, that the main source of decoherence is thermal relaxation, and consider a simple Markovian model for it. Additionally, we consider this infidelity to be independent for each qubit, and also independent from their unitary dynamics. Therefore, the total fidelity of the computation is given by

$$F_{\text{total}} \approx \langle F_{\text{U}} \rangle \times \mathrm{e}^{-Nt/T_1}, \tag{J1}$$

where F_{U} is the unitary evolution's fidelity, as defined in equation (28) and represented in figure 5(b), N is the number of qubits, t is the execution time of the quantum circuit and T_1 is the thermal relaxation time. While approximate, this expression can give us insight into the interplay between the scaling of the two sources of infidelity.

In order to extend $\langle F_{\text{U}} \rangle$ to a higher number of qubits, for which the effects of decoherence become more relevant, we fit the fidelity data of figure 5(e) for DQC, sDAQC and bDAQC to a function of the form

$$\langle F_{\text{U}} \rangle \approx f^{a\left(N^b\right)} + c, \tag{J2}$$

where we have assumed that each operation incurs in an independent infidelity, and where f, a, b, c are the parameters resulting from the function fitting, which are given in table 2. We plot the fitted curves on top of the simulated data in figure 11.

Finally, in figure 12, we plot the resulting total fidelity calculated as in equation (J1) for different scenarios, in which TQGs have execution times of 50, 150 and 300ns, and in which T_1 is either 50 or 500 μs. For the regime in which T_1 is very short, and the time of the TQGs is very long, the trade-off is favorable to DAQC, as can be seen in figure 12(b), for which $T_1 = 50\,\mu$s, and DAQC outperforms DQC for $t_{\text{TQG}} = 150$ ns and $t_{\text{TQG}} = 300$ ns.

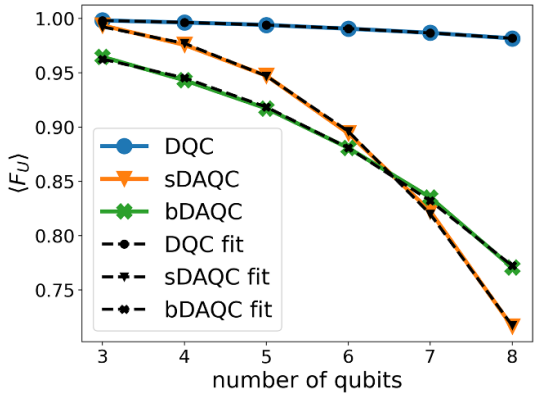

Figure 11. Average fidelity of the star-QFT algorithm for DQC, sDAQC and bDAQC, considering control errors, obtained in section 5. The dashed lines represent the fitted curves of the form (J2).

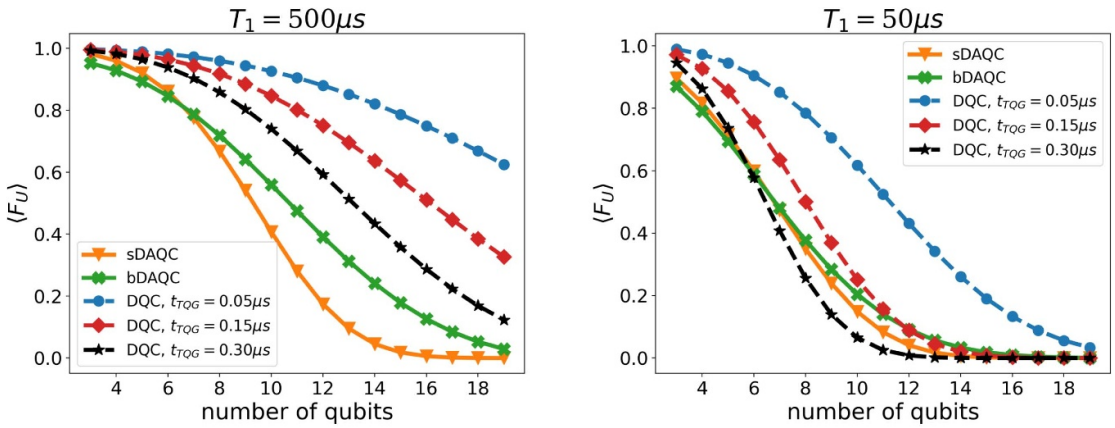

Figure 12. Approximate total fidelity of the star-QFT algorithm, calculated according to equation (J1), in the DQC, sDAQC and bDAQC paradigms, for different execution times of the TQGs, and (a) a relatively large $T_1 = 500\,\mu s$, and (b) a relatively small $T_1 = 50\,\mu s$. The trade-off between control errors and decoherence can be favorable to DAQC in a parameter regime with very limited T_1 and very long TQGs, as can be seen in (b), where DAQC outperforms DQC for $N > 11$ when $t_{\mathrm{TQG}} = 0.15\,\mu s$, and for $N > 5$ when $t_{\mathrm{TQG}} = 0.3\,\mu s$.

ORCID iDs

Vicente Pina Canelles https://orcid.org/0000-0002-8595-9581
Mario Ponce https://orcid.org/0000-0003-3541-5196

References

[1] Parra-Rodriguez A, Lougovski P, Lamata L, Solano E and Sanz M 2020 *Phys. Rev. A* **101** 022305
[2] Garcia-de Andoin M, Saiz A, Pérez-Fernández P, Lamata L, Oregi I and Sanz M 2024 *Phys. Rev. Res.* **6** 013280
[3] Galicia A, Ramon B, Solano E and Sanz M 2020 *Phys. Rev. Res.* **2** 033103
[4] Martin A, Lamata L, Solano E and Sanz M 2020 *Phys. Rev. Res.* **2** 013012
[5] García-Molina P, Martin A, Garcia de Andoin M and Sanz M 2024 *Commun. Phys.* **7** 321
[6] Martin A, Ibarrondo R and Sanz M 2023 *Phys. Rev. Appl.* **19** 064056
[7] Headley D, Müller T, Martin A, Solano E, Sanz M and Wilhelm F K 2022 *Phys. Rev. A* **106** 042446
[8] Lamata L, Parra-Rodriguez A, Sanz M and and E S 2018 *Adv. Phys. X* **3** 1457981
[9] Ezratty O 2023 Where are we heading with nisq? (arXiv:2305.09518)
[10] Baßler P, Zipper M, Cedzich C, Heinrich M, Huber P H, Johanning M and Kliesch M 2023 *Quantum* **7** 984
[11] Werninghaus M, Egger D J, Roy F, Machnes S, Wilhelm F K and Filipp S 2021 *npj Quantum Inf.* **7** 14
[12] Sung Y *et al* 2021 *Phys. Rev. X* **11** 021058
[13] Chu J and Yan F 2021 *Phys. Rev. Appl.* **16** 054020
[14] Hangleiter D, Roth I, Fuksa J, Eisert J and Roushan P 2024 *Nat. Commun.* **15** 9595
[15] Wendin G 2017 *Rep. Prog. Phys.* **80** 106001
[16] Yu J, Retamal J C, Sanz M, Solano E and Albarrán-Arriagada F 2022 *EPJ Quantum Technol.* **9** 9
[17] Yu W, Sun J, Han Z and Yuan X 2023 *Quantum* **7** 1045

[18] Wilde F, Kshetrimayum A, Roth I, Hangleiter D, Sweke R and Eisert J 2022 Scalably learning quantum many-body hamiltonians from dynamical data (arXiv:2209.14328 [quant-ph])
[19] Granade C E, Ferrie C, Wiebe N and Cory D G 2012 *New J. Phys.* **14** 103013
[20] Arute F *et al* 2019 *Nature* **574** 505
[21] Fischer M H, Maksymenko M and Altman E 2016 *Phys. Rev. Lett.* **116** 160401
[22] Johri S, Nandkishore R and Bhatt R N 2015 *Phys. Rev. Lett.* **114** 117401
[23] Glicenstein A, Ferioli G, Browaeys A and Ferrier-Barbut I 2022 *Opt. Lett.* **47** 1541
[24] Žnidarič M 2015 *Phys. Rev. E* **92** 042143
[25] Masson S J and Asenjo-Garcia A 2022 *Nat. Commun.* **13** 2285
[26] Parmee C D and Ruostekoski J 2020 *Commun. Phys.* **3** 205
[27] Scheibner M, Schmidt T, Worschech L, Forchel A, Bacher G, Passow T and Hommel D 2007 *Nat. Phys.* **3** 106
[28] Lambert N, Matsuzaki Y, Kakuyanagi K, Ishida N, Saito S and Nori F 2016 *Phys. Rev. B* **94** 224510
[29] Zhang Y, Yu L, Liang J Q, Chen G, Jia S and Nori F 2014 *Sci. Rep.* **4** 4083
[30] Nielsen M A and Chuang I L 2010 *Quantum Computation and Quantum Information* (Cambridge University Press)
[31] Greenberger D M 2009 Ghz (greenberger—horne—zeilinger) theorem and ghz states *Compendium of Quantum Physics* ed D Greenberger, K Hentschel and F Weinert (Springer Berlin Heidelberg) pp 258–63
[32] Ghosh J 2011 A note on the measures of process fidelity for non-unitary quantum operations (arXiv:1111.2478 [math-ph])
[33] Krantz P, Kjaergaard M, Yan F, Orlando T P, Gustavsson S and Oliver W D 2019 *Appl. Phys. Rev.* **6** 021318
[34] McKay D C, Wood C J, Sheldon S, Chow J M and Gambetta J M 2017 *Phys. Rev. A* **96** 022330
[35] Qiskit contributors 2023 Qiskit: an open-source framework for quantum computing *Zenodo* (https://10.5281/zenodo.2573505)
[36] Carignan-Dugas A, Wallman J J and Emerson J 2019 *New J. Phys.* **21** 053016
[37] Daley A, Bloch I, Kokail C, Flannigan S, Pearson N, Troyer M and Zoller P 2022 *Nature* **607** 667
[38] Arrazola I n, Pedernales J S, Lamata L and Solano E 2016 *Sci. Rep.* **6** 30534
[39] Babukhin D V, Zhukov A A and Pogosov W V 2020 *Phys. Rev. A* **101** 052337
[40] Céleri L C, Huerga D, Albarrán-Arriagada F, Solano E, Garcia de Andoin M and Sanz M 2023 *Phys. Rev. Appl.* **19** 064086
[41] Tao Z *et al* 2021 *npj Quantum Inf.* **7** 73
[42] Gonzalez-Raya T, Asensio-Perea R, Martin A, Céleri L C, Sanz M, Lougovski P and Dumitrescu E F 2021 *PRX Quantum* **2** 020328
[43] Guseynov N M and Pogosov W V 2022 *J. Phys.: Condens. Matter* **34** 285901
[44] Huang K *et al* 2021 *npj Quantum Inf.* **7** 165
[45] Michel A, Grijalva S, Henriet L, Domain C and Browaeys A 2023 *Phys. Rev. A* **107** 042602
[46] Gong M *et al* 2023 *Sci. Bull.* **68** 906
[47] Dodd J L, Nielsen M A, Bremner M J and Thew R T 2002 *Phys. Rev. A* **65** 040301
[48] Suzuki M 1976 *Commun. Math. Phys.* **51** 183
[49] Lloyd S 1996 *Science* **273** 1073
[50] Jordan P and Wigner E 1928 *Z. Phys.* **47** 631
[51] Algaba M G, Sriluckshmy P V, Leib M and Simkovic F 2023 Low-depth simulations of fermionic systems on square-grid quantum hardware (arXiv:2302.01862)
[52] Ba nuls M C *et al* 2020 *Eur. Phys. J. D* **74** 165
[53] Lechner W, Hauke P and Zoller P 2015 *Sci. Adv.* **1** e1500838
[54] Lechner W 2020 *IEEE Trans. Quantum Eng.* **1** 1
[55] Sriluckshmy P V, Pina-Canelles V, Ponce M, Algaba M G, Šimkovic F IV and Leib M 2023 *Quantum Sci. Technol.* **8** 045029
[56] Acharya R *et al* 2024 *Nature* **638** 920–6
[57] Kim Y *et al* 2023 *Nature* **618** 500
[58] Yan F, Krantz P, Sung Y, Kjaergaard M, Campbell D L, Orlando T P, Gustavsson S and Oliver W D 2018 *Phys. Rev. Appl.* **10** 054062
[59] McKay D C, Hincks I, Pritchett E J, Carroll M, Govia L C G and Merkel S T 2023 Benchmarking quantum processor performance at scale (arXiv:2311.05933 [quant-ph])
[60] Abdurakhimov L *et al* 2024 Technology and performance benchmarks of iqm's 20-qubit quantum computer (arXiv:2408.12433 [quant-ph])
[61] Collodo M C, Herrmann J, Lacroix N, Andersen C K, Remm A, Lazar S, Besse J-C, Walter T, Wallraff A and Eichler C 2020 *Phys. Rev. Lett.* **125** 240502
[62] Berke C, Varvelis E, Trebst S, Altland A and DiVincenzo D P 2022 *Nat. Commun.* **13** 2495
[63] Marxer F *et al* 2023 *PRX Quantum* **4** 010314
[64] Fowler A G, Devitt S J and Hollenberg L C L 2004 *Quantum Inf. Comput.* **4** 237–51
[65] Maslov D 2007 *Phys. Rev. A* **76** 052310
[66] Algaba M G, Ponce-Martinez M, Munuera-Javaloy C, Pina-Canelles V, Thapa M J, Taketani B G, Leib M, de Vega I, Casanova J and Heimonen H 2022 *Phys. Rev. Res.* **4** 043089